Physical and Data-Driven Models Hybridisation for Modelling the Dynamic State of a Four-Stroke Marine Diesel Engine

Coraddu, Andrea; Kalikatzarakis, Miltiadis; Theotokatos, Gerasimos; Geertsma, Rinze; Oneto, Luca

Citation (APA)
Coraddu, A., Kalikatzarakis, M., Theotokatos, G., Geertsma, R., & Oneto, L. (2022). Physical and Data-Driven Models Hybridisation for Modelling the Dynamic State of a Four-Stroke Marine Diesel Engine. In A. Kumar Agarwal, D. Kumar, N. Sharma, & U. Sonawane (Eds.), *Engine Modeling and Simulation* (pp. 145-193). (Energy, Environment, and Sustainability). Springer. https://doi.org/10.1007/978-981-16-8618-4_6

Important note
To cite this publication, please use the final published version (if applicable).
Please check the document version above.

Chapter 6
Physical and Data-Driven Models Hybridisation for Modelling the Dynamic State of a Four-Stroke Marine Diesel Engine

Andrea Coraddu , **Miltiadis Kalikatzarakis** , **Gerasimos Theotokatos** , **Rinze Geertsma** , **and Luca Oneto**

Abstract Accurate, reliable, and computationally inexpensive models of the dynamic state of combustion engines are a fundamental tool to investigate new engine designs, develop optimal control strategies, and monitor their performance. The use of those models would allow to improve the engine cost-efficiency trade-off, operational robustness, and environmental impact. To address this challenge, two state-of-the-art alternatives in literature exist. The first one is to develop high fidelity physical models (e.g., mean value engine, zero-dimensional, and one-dimensional models) exploiting the physical principles that regulate engine behaviour. The second one is to exploit historical data produced by the modern engine control and automation systems or by high-fidelity simulators to feed data-driven models (e.g., shallow and deep machine learning models) able to learn an accurate digital twin of the system without any prior knowledge. The main issues of the former approach are its complexity and the high (in some case prohibitive) computational require-

M. Kalikatzarakis · G. Theotokatos
Department of Naval Architecture, Ocean and Marine Engineering, University of Strathclyde, Glasgow, UK
e-mail: miltiadis.kalikatzarakis@strath.ac.uk

G. Theotokatos
e-mail: gerasimos.theotokatos@strath.ac.uk

A. Coraddu (✉) · R. Geertsma
Department of Maritime and Transport Technology, Delft University of Technology, Delft, The Netherlands
e-mail: a.coraddu@tudelft.nl

R. Geertsma
e-mail: r.d.geertsma@tudelft.nl;rd.geertsma@mindef.nl

L. Oneto
DIBRIS, University of Genova, Genoa, Italy
e-mail: luca.oneto@unige.it

R. Geertsma
Department of Military Systems & Technology, Netherlands Defence Academy, Breda, The Netherlands

145

ments. While the main issues of the latter approach are the unpredictability of their behaviour (guarantees can be proved only for their average behaviour) and the need for large amount of historical data. In this work, following a recent promising line of research, we describe a modelling framework that is able to hybridise physical and data driven models, delivering a solution able to take the best of the two approaches, resulting in accurate, reliable, and computationally inexpensive models. In particular, we will focus on modelling the dynamic state of a four-stroke diesel engine testing the performance (both in terms of accuracy, reliability, and computational requirements) of this solution against state-of-the-art physical modelling approaches on real-world operational data.

6.1 Introduction

In recent years the maritime industry has been challenged by several issues. The volatile bunker prices affect cargo transportation costs and the shipowners' competitiveness and operations viability (García-Martos et al. 2013). Strict regulations are in place to limit emissions (Committee 2011) with the aim of reducing CO_2 emissions from shipping by 40–50% (Commission 2013a, b). As a result of this combination, energy efficiency and environmental sustainability of maritime operations are currently the primary challenges to be faced by the maritime industry. Shipowners and operators are adopting several measures to lower fuel consumption and associated emissions (Chiong et al. 2021; Lion et al. 2020), and researchers in the field are developing innovative technologies and methods that can increase the environmental efficiency and cost-effectiveness of ship operations (Xing et al. 2020; Ni et al. 2020).

Improvements in energy efficiency can be obtained by a variety of design and retrofit measures (Lindstad et al. 2015; Gucwa and Schäfer 2013), such as hull design optimisation (Tillig et al. 2015; Lindstad and Eskeland 2015), adoption of alternative fuels (Chiong et al. 2021), and alternative energy sources (Bouman et al. 2017), as well as operational measures (Zis and Psaraftis 2018; Xing et al. 2020), including speed optimisation (Wen et al. 2017; Fagerholt and Psaraftis 2015; Psaraftis and Kontovas 2014), better capacity utilisation (Xing et al. 2020), and advanced route planning execution methods (Yu et al. 2021; Zis et al. 2020).

Nevertheless, it is widely known that for the majority of the vessels operating today, the main engines and to a lesser extent the auxiliary engines are the main factors of energy losses (Baldi et al. 2014, 2015). For this reason, engine manufacturers are focusing on further increasing Diesel Engine (DE) power density and enhancing operating performance (Lion et al. 2020).

Identifying and adopting new technologies in marine DEs is limited by the expensive design (Baldi et al. 2015), prototyping and experimentation processes (Kamal

and Hui 2013). To mitigate these issues, computational models have been developed to simulate the physical processes occurring in a DE under steady-state (Larsen et al. 2015) and transient conditions (Theotokatos and Kyrtatos 2003) as a rapid and cost-effective prototyping tool (Merker et al. 2005). A common effort in the development of all computational models is towards improving their accuracy and reliability (Oberkampf and Trucano 2002). As such, the model verification, calibration, and validation processes occupy a central role, based on which the predictive capabilities of the model are assessed to justify its use for the application of interest (Oberkampf et al. 2004).

In the literature it is possible to find three main approaches to the DEs: Physical Models (PMs), Data-Driven Models (DDMs), and Hybrid Models (HMs). PM requires a deep knowledge of the physical phenomena (Grimmelius 2003; Grimmelius et al. 2007). The higher is the detail in the modelling of the equations which describe the physical phenomena, the higher is the expected accuracy of the results and the computational time required for the simulation. The second approach, instead, infers the desired model directly from historical data collected by on board machinery and does not require any a-priori knowledge of the underlying physical phenomena (Coraddu et al. 2021a). However, since these models are not supported by any physical interpretation, they need a significant amount of data to be built. The third approach is a combination of the previous ones and it is based on the integration of a PM and DDM into a single model. The DDM model compensates for the secondary effects not modelled by the PM and the PM helps the DDM in reducing the amount of historical data required to train it (Oneto et al. 2016).

A literature review on PMs, DDMs, and HMs for DE is reported in Sect. 6.2 showing that a complete and clear description of a modelling framework able to hybridise PMs and DDMs is not yet readily available. For this reason, this chapter is devoted to the presentation of this framework combining the computational efficiency of the 0D PM with the level of accuracy of the DDM.

With this goal in mind, first a 0D DE model will be proposed and validated for both steady-state and transient operations. This analysis will underline the high predictive capabilities of the PM in steady-state operations, and will also reveal the limited predictive capabilities under transient operation. Subsequently, different DDMs will be developed, tested, and compared. These models will leverage the information encapsulated in historical data to produce accurate predictions on a set of performance parameters of the DE. Finally, we will present the hybridisation framework where a set of HMs will be proposed, leveraging on both the DDMs and the PM previously developed. The authors will showcase the performance in terms of accuracy, reliability, and computational requirements of the HMs, clearly demonstrating the superiority of the proposed hybridisation framework on a comprehensive dataset containing real operational data from a marine DE for a time period of approximately 3 years.

The rest of the paper is organised as follows. Section 6.2 presents the state-of-the-art in PMs, DDMs, and HMs for marine DEs. Section 6.3 describes the hybridisation framework, starting from the theory of the PMs and DDMs and then going into the details of the HMs. Section 6.4 presents a specific DE case study and the related

historical data available. Section 6.5 demonstrates the advantages and disadvantages of the different approaches presented in Sect. 6.3. Section 6.6 concludes this work.

6.2 Related Work

This section is devoted to the review of PMs, DDMs, and HMs for marine DEs. Note that the models can be categorised also according to other criteria (Grimmelius 2003). The choice that we made reflects the experience and knowledge on the subject.

6.2.1 Physical Models

PMs are the most traditional models for DE development, design, optimisation, and performance evaluation with extensive work carried out over several decades (Grimmelius et al. 2007). Many insightful reviews on this subject can be found (Grimmelius et al. 2007; Geertsma et al. 2017; Merker et al. 2005). All these reviews agree on the fact that the choice of the most suitable model strongly depends on the scope of work, the application requirements, and the available computational tools (Johnson et al. 2010). In general, to the best of the authors knowledge, PMs achieve errors well within the tolerance margins provided by engine manufacturers in steady state conditions, whereas reported results during transient operations tend to be less accurate.

Among PMs, Mean Value Engine Models (MVEMs) are a common choice when low computational effort is required (Maroteaux and Saad 2015; Guzzella and Onder 2009; He and Lin 2007; Lee et al. 2013; Miglianti et al. 2020, 2019). MVEMs are approximate first-principle models that adequately predict engine performance parameters, and are prevalent in applications in which the engine is considered as just one component of a wider system, or for control strategies development (Malkhede et al. 2005; Guan et al. 2014; Theotokatos 2010; Grimmelius et al. 2010; Theotokatos 2008; Nikzadfar and Shamekhi 2015; Geertsma et al. 2017; Theotokatos et al. 2018; Geertsma et al. 2018; Guzzella and Onder 2009).

MVEM can be classified in the following two categories: (a) not considering the engine manifolds dynamics; (b) including the engine manifold dynamics. Category (a) employs only two differential equations for calculating the engine and TC rotational speeds. Category (b) employs additional equations to calculate the pressure and temperature of the engine manifolds. MVEMs employ simpler approaches to estimate the engine parameters on an engine cycle basis. These models are employed in cases where calculations of low computational cost are required, with the most common example being the engine control system design.

0D models employ a more detailed formulation and are capable of predicting the in-cycle variations of the engine parameters. The latter are employed in the cases where the in-cylinder parameters (pressure, temperature, composition) variations are

required leading to a more accurate estimation of the engine performance parameters. For instance, Llamas and Eriksson (2018) developed a control-oriented MVEM for a large two-stroke engine with Exhaust Gas Recirculation (EGR), with relative errors under 3.35% for steady state operations. A similar study was performed by the authors of Dahl et al. (Dahl et al. 2018), who also developed an MVEM for control strategy design, reporting errors smaller than 5% for all engine parameters under steady state conditions. In both these studies (Llamas and Eriksson 2018; Dahl et al. 2018), the authors did not report results under transient operation, nevertheless general trends of the real engine parameters were adequately captured. The authors of Sui et al. (2017) exploited an MVEM to investigate the performance of a medium-speed DE during preliminary design. The results of the in-cylinder process showed good correspondence with the test data across all process parameters, including in-cylinder temperatures, with satisfactory accuracy and adaptability to variable operating conditions. Authors of Sapra et al. (2017) studied back pressure effects on the performance of a marine DE, by means of an MVEM. Although quantitative performance metrics for the model are not reported, the graphical representation of the results indicates average relative percentage errors of around 4% for the turbine inlet temperature across all operating conditions.

More sophisticated approaches, with respect to MVEMs, are zero-dimensional (0D), one-dimensional (1D), and three-dimensional (3D) models that operate on a per-crank basis (Merker et al. 2005). These approaches are more computationally demanding compared to MVEMs, however they can predict the detailed gas processes inside the cylinders (Mohammadkhani et al. 2019; Stoumpos et al. 2018, 2020). For instance, authors of Guan et al. (2015) investigated a two-stroke marine DE with emphasis on part load operating conditions using a 0D model validated against experimental data obtained from engine shop tests in steady state operations. Very small errors were reported for loads between 25–100%, ranging between 0.6–2%. Authors of Larsen et al. (2015) also developed a 0D model, with a similar validation approach, reporting a root mean square deviation of approximately 1% across all engine performance parameters. Authors of Sapra et al. (2020) compared the capabilities of Seiliger-based and double Wiebe function-based 0D models to capture hydrogen-natural gas combustion in a marine engine for different fuel blends and engine loads. In this study, very small errors were reported for in-cylinder process parameters, ranging between 0.1–2.4%.

Several attempts to combine MVEM and 0D, 1D, or 3D models have been proposed, enhancing the predictive abilities of MVEMs with lower computational requirements than their 0D, 1D, or 3D counterparts (Livanos et al. 2007; Ding et al. 2010; Baldi et al. 2015; Maroteaux and Saad 2015; Tang et al. 2017).

In fact, in cases where low computational cost is required whilst the predictive capability for the engine in-cylinder parameters must be retained, approaches combining MVEMs and 0D models have been employed. In such cases, one engine cylinder (typically the closed cycle) is modelled by employing the 0D approach and interfaced with the MVEM. This provides the advantage of negating the extensive calibration process of the MVEM (which is typically based on data derived from either experiments or simulations with more detailed models) required to predict the

engine performance parameters. For instance, authors of Baldi et al. (2015) combined MVEM and 0D models to investigate the propulsion behaviour of a handymax-size product carrier under constant and variable engine speed operations. The model was validated against experimental data from the engine's shop tests, for loads ranging between 50–110%. High accuracy was reported, with errors ranging between 1.9–2.7%. Furthermore, the authors concluded that their proposal provides a favourable time-accuracy trade-off and it can be used in cases where information, not provided by an MVEM, is required.

The integration of a 1D with a Computational Fluid Dynamics (CFD) based 3D model was proposed by the authors of Wang et al. (2020). The authors conducted a parametric investigation of a large four-stroke dual-fuel marine DE to identify the pre-injection effects on the engine combustion, knocking, and emission parameters. This modelling approach was validated under steady-state conditions in four operating points within a range of 25–100% of the nominal load. Near-zero deviation was reported for most parameters, whereas the maximum deviation for NOx emissions was about 2%. Finally, the authors of Hao et al. (2021) aimed to improve the in-cylinder fuel/air mixing process of heavy-duty DEs, which they modelled utilising CFD methods. Their simulations were validated in terms of the spray liquid/vapour penetration, heat release rate, and in-cylinder pressures, at various operational, and environmental conditions, reporting very low discrepancies.

When it comes to computational requirements, MVEMs are calibrated by using data from measurements or more detailed models. They typically exhibit absolute errors of less than 2%. However, outside the calibration envelope, their performance deteriorates. For 0D/1D models (where 0D refers to modelling the in-cylinder pro-cesses or volumes, whereas 1D refers to the modelling of pipes and manifolds), the expected typical errors are in the range of $\pm 5\%$. The more significant errors are exhibited for predicting the exhaust gas temperature and emissions, whereas errors for the other engine performance parameters are typically in the range $\pm 3\%$. Finally, evaluating the error is challenging for CFD models as the available measured param-eters are pretty limited in most cases (typically the in-cylinder pressure diagram). However, the model set-up process consists of several steps (geometry, injection and mixing process, meshing studies in fixed combustion chambers (bombs), testing of various existing sub models) culminating in the set up of the final model version. In addition, several quantitative verification studies are typically carried out, thus providing confidence to the users that the model performance is appropriate.

We can conclude then that PMs can adequately capture most process parameters of a DE under a broad range of operating conditions. However, there is a clear trade-off between accuracy and computational requirements. In fact, the most detailed 3D models cannot run in real-time, whereas MVEMs lack accuracy, especially during transient operations.

6.2.2 Data-Driven Models

DDMs have been successfully applied in a variety of maritime applications, provided that the necessary quality and quantity of historical data is actually available (Coraddu et al. 2016, 2017, 2019, 2020, 2019, 2021a, b; Cipollini et al. 2018a, b; Stoumpos et al. 2020).

For instance, the Nikzadfar and Shamekhi (2014) developed an Artificial Neural Network (ANN) to study the relative contribution of several operating parameters to the performance of a DE. The authors utilised 4000 steady-state operating points to train the ANN, generated by means of numerical simulation, covering the entire envelope of the DE. Although the authors did not provide quantitative results regarding the model accuracy, graphical representation showed a relative difference of approximately 5%. Authors of Shin et al. (2020) developed an ANN to predict the NO_x emissions of a DE under transient operation. Highly accurate results were reported, with the developed ANN being able to predict NO_x with errors around 1.6%, comparable to the accuracy of physical NO_x measurement devices, with typical error margins of 1%. The ability of ANNs to predict performance parameters of a DE was also demonstrated by the authors of Ozener et al. (2013) predicting a variety of performance parameters and emissions with coefficient of determination (R^2) values over 0.95. A hydrogen dual-engine for automotive applications was the case study of the authors of Syed et al. (2017): ANNs proved to be extremely efficient, with near-zero errors being reported for the prediction of specific fuel consumption and a variety of emissions. A similar study was conducted by the authors of Liu et al. (2018) employing an ANN to predict the emissions and various performance parameters of a spark ignition engine fueled with butanol-gasoline blends. In this study, ANNs were able to predict the performances of the engine with very high R^2 values.

DDMs are frequently used in the field of condition monitoring of DEs, as they are extremely efficient at detecting and isolating faults and have proven to increase the reliability and decrease the probability of producing false alarms (Ahmed et al. 2015). For instance, authors of Namigtle-Jimenez (2020) developed 3 ANNs for fault detection and diagnosis of a DE, utilising only the pressure signal of the injection rail. They demonstrated that the proposed ANNs were able to detect and isolate the faulty injector of the electronic fuel system with 100% classification accuracy in offline training scenarios and near 100% accuracy in online scenarios. The authors of Wang et al. (2021) proposed a random convolutional ANN for health monitoring of DEs, relying on vibration measurements. Considering the very high accuracy of the developed ANN on this task, the authors concluded that, compared to traditional methods based on signal analysis techniques and shallow classifiers, their approach can automatically learn high-level representative features from the raw vibration signals and eliminate the necessity of the time-consuming manual feature extraction. A similar study was performed by the authors of Wang et al. (2019) presenting a Bayesian ANN-based approach for fault isolation in a DE fuel injection system under the presence of uncertainties. With the proposed approach, the authors demonstrated that symptoms under multiple faults could be decoupled into symptoms correspond-

ing to each individual fault. This greatly reduced the prior knowledge needed for the diagnosis, decreased the complexity of the application, and significantly improved computational efficiency. The authors of Palmer and Bollas (2019) demonstrated the ability of DDMs to predict and isolate faults. More specifically, the authors showed that when proper fault detection and isolation test designs are selected, even the relatively simple combination of principal component analysis and k-nearest neighbours classifier could provide satisfactory results in fault detection. Likewise, the authors of Ahmed et al. (2015) trained an ANN employing a new estimation strategy known as the smooth variable structure filter to detect the engine's faults. This approach demonstrated stability and generalisation accuracy exhibiting improved performance compared with the first order back propagation algorithm and similar performance compared with the extended Kalman filter. Fault detection was also the scope of the work of the authors of Wang et al. (2020) where a noise-based method based on ANNs and wavelet packet analysis was presented. The authors concluded that ANNs are effective for feature extraction of engine fault noises in time and frequency domains, and are powerful for sound feature classification and recognition of the engine's faults. A further example is reported by the authors of Coraddu et al. (2021b) where multiple DDMs for weakly supervised marine dual fuel engines health monitoring were designed, presented, and tested. The proposed framework relied on a digital twin of the engine or on novelty detection algorithms which were compared against state-of-the-art fully supervised approaches. Utilising data from the validated simulation model of Stoumpos et al. (2020), the authors demonstrated that their approach can overcome the problematic requirement for a large amount of labelled samples, that are rarely available, with a decrease in performance of less than 1% compared to state-of-the-art fully-supervised approaches.

6.2.3 Hybrid Models

HMs are a quite recent modelling approach, especially in the maritime field, and just very few works showed the advantages of a hybrid approach, with respect to pure PMs and DDMs (Coraddu et al. 2021a, 2018; Miglianti et al. 2019, 2020). For instance, in Coraddu et al. (2017) the authors show that it is possible to effectively predict fuel consumption with HMs. Moreover, in Coraddu et al. (2018, 2021a), the authors also attempted to model the engine exhaust gas temperature with HMs under steady state and transient conditions.

Authors of Mishra and Subbarao (2021) compared the performance of a PM, a DDM, and an HM to predict dynamic combustion control parameters of a Reactivity Controlled Compression Ignition engine across five engine loads. The parameters included the start of combustion, the 50% mass fraction burnt crank angle, and combustion peak pressure. The authors compared the model predictions with measured data from experiments, concluding that the prediction capability of the HM was far superior to the DDM and PM across all parameters.

Authors of Bidarvatan et al. (2014) developed an HM to predict several performance parameters of Homegeneous Charge Compression Ignition (HCCI) engines. Namely, the the 50% mass fraction burnt crank angle, the indicated mean effective pressure, exhaust temperature, and concentration of CO, total unburned hydrocarbons and NO_x. The proposed HM combined a PM and 3 ANNs, designed to minimise computational time requirements, with minimal sacrifice in accuracy. The authors compared the predictions of the proposed HM with experimental data at 309 steady state and transient conditions for two HCCI engines, concluding that the HM offered approximately 80% better accuracy compared to the PM, or 60% compared to the DDM.

As expected, the amount of literature available on the HMs is limited, being this a relatively new and still partially explored research field. Moreover, focusing on the marine DE applications, to the authors best knowledge, a complete and clear description of a modelling framework for marine DEs able to hybridise PMs and DDMs is not yet readily available.

6.3 Modelling

This section is devoted first to the presentation of a state-of-the-art 0D PM (see Sect. 6.3.1) and DDM (see Sect. 6.3.2). Then the hybridisation framework is presented together with the proposed HM (see Sect. 6.3.3).

6.3.1 Zero Dimensional Diesel Engine Model

The DE PM has been developed utilising a modular approach, in which the engine scavenging air and exhaust gas receivers are modelled as control volumes, whereas the compressor and turbine are modelled as flow elements. The exhaust receiver contains states for pressure p, temperature T, and exhaust gas composition $\boldsymbol{g}$. The gas composition of the air path has been assumed constant. The engine boundaries are modelled using fixed fluid elements of constant pressure and temperature, and shaft elements are utilised to compute the rotational speed of the turbocharger ω_{tc} and crankshaft ω_e. Finally, for the in-cylinder process we exploited a two-zone 0D approach, with state quantities being the in-cylinder pressure, temperature, gas composition, and air-fuel equivalence ratio λ for each zone. The layout and state variables of the developed model are presented in Fig. 6.1. The governing equations of all relevant components is discussed in the the following.

Gas composition and properties—The working fluid of the engine is considered to be a mixture of the following 11 species: CO_2, H_2O, N_2, O_2, CO, H_2, O, H, OH, NO, and N. As such, the concentration vector in an arbitrary control volume is defined as
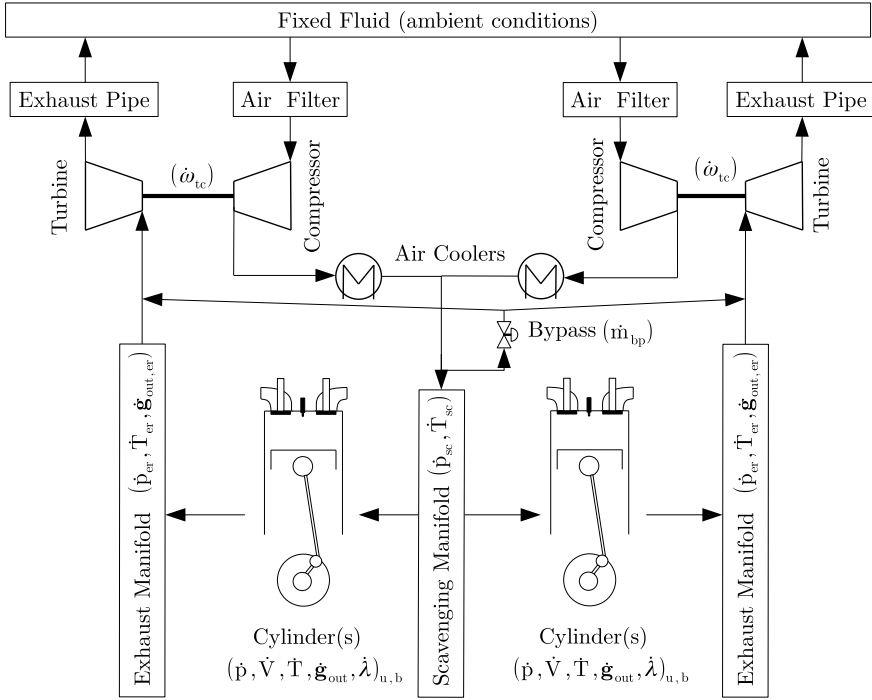
Fig. 6.1 Layout of the PM with all relevant components and state variables

$$g = \frac{\left[m_{CO_2}, m_{H_2O}, m_{N_2}, m_{O_2}, m_{CO}, m_{H_2}, m_O, m_H, m_{OH}, m_{NO}\right]}{m_{tot}}, \quad (6.1)$$

where m_i is the mass flow of species i and $m_{\text{tot}} = \sum_{i=1}^{11} m_i$. Arbitrarily, N is not included in the concentration vector since it can be computed as the remaining part, to ensure that the mass conservation law is not violated and to act as a sanity check of the numerical integration.

The thermodynamic properties of the gas are calculated using the NASA polynomials (McBride et al. 2002), under the assumption of a thermally perfect gas. The concentration along the air path is assumed constant and equal to the standard air concentration.

Control Volumes—The control volumes are modelled using the open thermodynamic system concept (Watson and Janota 1982; Heywood 1988) which use as inputs p, T, and the composition of the working medium contained in the adjacent elements. Considering the control volumes as cylindrical solenoids (neglecting dissociation effects and the kinetic energy of the flows entering/exiting the receivers) and assuming ideal gas, the change of rate in the mass stored in the volume m can be expressed as

$$\frac{\mathrm{d}m}{\mathrm{d}t} = \sum_i \dot{m}_{\mathrm{in},i} - \sum_j \dot{m}_{\mathrm{out},j}, \tag{6.2}$$

where $\dot{m}_i$ is the mass flow rate of stream i and the subscripts in, out refer to flows entering and exiting the control volume respectively. Note that, the mass rate of change does not need to be integrated since it only represents the difference between entering and exiting mass flow rates.

The temperature rate of change is derived from the energy conservation as

$$\frac{\mathrm{d}T}{\mathrm{d}t} = \frac{\dot{Q} + \sum_i mh_{\mathrm{in},i} - \sum_j mh_{\mathrm{out},j} - u\frac{\mathrm{d}m}{\mathrm{d}t}}{mc_v}, \tag{6.3}$$

where mh refers to the enthalpy flow rate (entering $mh_{\mathrm{in},i}$ and exiting $mh_{\mathrm{out},i}$ for the stream i), $\dot{Q} = kA(T - T_{\mathrm{amb}})$ represents the heat transfer from the control volume to the surrounding environment, with k being the heat transfer coefficient, $A = \pi d^2/4$ being the heat transfer area, and u is the internal energy.

The heat transfer coefficient can be computed as (Merker et al. 2005)

$$k = 0.024\frac{\kappa}{d}\left[1 - \left(\frac{d}{l}\right)^{\frac{2}{3}}\right]\mathrm{Re}^{0.786}\mathrm{Pr}^{0.45}, \tag{6.4}$$

where l and d refer to the length and inner diameter of the control volume and κ being the heat conductivity, evaluated as

$$\kappa = 3.65182 \ 10^{-4}T^{0.748}. \tag{6.5}$$

The Prandtl number Pr has been kept constant and equal to 0.731 and the Reynolds number Re is evaluated on the average mass flow rate of the input and output streams $\dot{m}_{\mathrm{avg}}$ as

$$Re = \frac{\dot{m}_{\mathrm{avg}}d}{Av}, \tag{6.6}$$

with v being the kinematic viscosity computed as

$$v = 5.17791 \ 10^{-7}T^{0.62}. \tag{6.7}$$

Due to to the lack of information regarding the geometry of the control volumes, their inner diameters d and lengths l are considered as calibration parameters.

Moreover, considering the control volume as a well-stirred mixer, the dynamics of the concentration states can be derived as (Llamas and Eriksson 2019)

$$\frac{\partial \boldsymbol{g}_{\mathrm{out}}}{\partial t} = \frac{RT}{pV}\sum_j \left(\boldsymbol{g}_{\mathrm{in},j} - \boldsymbol{g}_{\mathrm{out}}\right)\dot{m}_{\mathrm{in},j}, \tag{6.8}$$

where $R = R(\boldsymbol{g}, T)$ is the gas mixture constant, V is the control volume, $\boldsymbol{g}_{\text{in},j}$ is the composition of gas of the input stream j, and $\boldsymbol{g}_{\text{out}}$ is the composition of gas of the output stream. Note that in the case of the scavenging air receiver, under the simplification of constant fresh air composition, these derivatives have been set to zero.

The pressure of the working medium contained in each control volume is calculated using the ideal gas law equation, from which the pressure's rate of change can be computed as

$$\frac{\mathrm{d}p}{\mathrm{d}t} = \frac{R}{V}\left(T\frac{\mathrm{d}m}{\mathrm{d}t} + m\frac{\mathrm{d}T}{\mathrm{d}t}\right). \tag{6.9}$$

Valves—The mass flow rate through a valve is computed assuming subsonic or sonic flow through a flow restriction (Heywood 1988), with the valve opening signal (lift) u_v as input

$$\dot{m}_v = A_{\text{eff}}(u_v)\frac{p}{\sqrt{RT}}\Psi, \quad \Psi = \begin{cases} \Pi^{\frac{1}{\gamma}}\sqrt{\frac{2\gamma}{\gamma-1}\left(1-\Pi^{\frac{\gamma-1}{\gamma}}\right)}, & \text{if } \Pi > \left(\frac{2}{\gamma+1}\right)^{\frac{\gamma}{\gamma-1}} \\ \sqrt{\gamma}\left(\frac{2}{\gamma+1}\right)^{\frac{\gamma+1}{2(\gamma-1)}}, & \text{otherwise} \end{cases}, \tag{6.10}$$

where u_v is chosen as the percentage lift of the valve, Π refers to the ratio of the static pressure downstream of the restriction to the upstream stagnation pressure, $\gamma = \gamma(\boldsymbol{g}, T)$ is the ratio of specific heats of the medium, and $A_{\text{eff}} = \mu(u_v)A_{\text{ref}}$ refers to the effective area of the valve computed as the product of a reference area A_{ref} with the appropriate flow coefficient $\mu(u_v)$ (Heywood 1988).

The bypass valve is assumed to be activated if the pressure on the compressor exceeds 90% of the surge limit for the instantaneous flow rate. Furthermore, we have assumed a linear opening characteristic, with the reference area considered as a calibration parameter. For the intake and exhaust valves, we utilised a non-linear characteristic, parameterised on the basis of the maximum cross-flow area of the inlet A_{iv} and exhaust valves A_{ev} and the crank-angle duration that the valve stays at its maximum lift denoted as vmd_{iv} and vmd_{ev} (Merker et al. 2005).

Air cooler, Air Filter, and Exhaust Pipe—Pressure losses in all these components, as well as air cooler effectiveness, have been modelled as quadratic functions of their corresponding input mass flow rate (Theotokatos 2010; Theotokatos et al. 2018)

$$\Delta p_{\text{ac}} = \sum_{i=0}^{2}\dot{m}_{\text{ac}}^{i}c_{\text{ac},i}, \quad \Delta p_{\text{af}} = \sum_{i=0}^{2}\dot{m}_{\text{af}}^{i}c_{\text{af},i},$$

$$\Delta p_{\text{ep}} = \sum_{i=0}^{2}\dot{m}_{\text{ep}}^{i}c_{\text{ep},i}, \quad \epsilon_{\text{ac}} = \sum_{i=0}^{2}\dot{m}_{\text{ac}}^{i}c_{\text{ac}_e,i}, \tag{6.11}$$

where the subscripts ac, af, and ep refer to the air cooler, air filter, and exhaust pipe, respectively. $c_{\text{ac},i}$, $c_{\text{af},i}$, c_{ep_i}, and $c_{\text{ac}_e,i}$ are considered calibration parameters.

As a consequence, the temperature at the air cooler outlet is given by

$$T_{\text{ac}}^{\text{out}} = \epsilon_{\text{ac}} T_w + (1 - \epsilon_{\text{ac}}) T_{\text{ac}}^{\text{in}}, \tag{6.12}$$

where ϵ_{ac} refers to the heat exchanger effectiveness, T_w corresponds to the temperature of the cooling water, and $T_{\text{ac}}^{\text{in}}$ is the temperature of the working medium at the inlet.

Turbocharger—The engine is equipped with two turbocharging units operating in parallel to supply the engine with sufficient air mass flow. We modelled the compressor using its steady state performance map, which provides the relations between the compressor performance variables: reference flow rate, pressure ratio, reference speed, and isentropic efficiency. The rotational speed and pressure ratio are considered as inputs to the model, which allows the computation of the reference flow rate $\dot{m}$ and isentropic efficiency η_c as reported in (Theotokatos and Tzelepis 2015; Baldi et al. 2015)

$$\dot{m} = f_{m_c}\left(\Pi_c, T_c^{\text{in}}, \omega_{\text{tc}}\right), \quad \eta_c = f_{\eta_c}\left(\Pi_c, T_c^{\text{in}}, \omega_{\text{tc}}\right), \tag{6.13}$$

where f_{m_c} and f_{η_c} are functions that have been interpolated based on the the compressor maps, representing the compressor mass flow rate and efficiency, respectively. Π_c is the pressure ratio of the compressor, and T_c^{in} is the compressor inlet temperature. After accounting for pressure losses in the air cooler and air filter, Π_c can be computed as

$$\Pi_c = \frac{p_{\text{sc}} + \Delta p_{ac}}{p_{\text{amb}} - \Delta p_{\text{af}}}, \tag{6.14}$$

where p_{sc} is the pressure of the scavenging receiver and p_{amb} is the ambient pressure. The temperature at the outlet of the compressor is given by (Watson and Janota 1982)

$$T_c^{\text{out}} = T_c^{\text{in}} \left(1 + \frac{\Pi_c^{\frac{\gamma-1}{\gamma}} - 1}{\eta_c}\right). \tag{6.15}$$

For the turbine, we exploited its swallowing capacity and efficiency maps, which allow the calculation of the turbine flow rate $\dot{m}_t$ and isentropic efficiency η_t as

$$\dot{m}_t = f_{m_t}\left(\Pi_t, T_t^{\text{in}}, \omega_{\text{tc}}\right), \quad \eta_t = f_{\eta_t}\left(\Pi_t, T_t^{\text{in}}, \omega_{\text{tc}}\right). \tag{6.16}$$

where f_{m_t} and f_{η_t} are functions that have been interpolated based on the the turbine maps, representing the turbine mass flow rate and efficiency, respectively. Π_t is the pressure ratio of the turbine, and T_t^{in} is the turbine inlet temperature. The turbine pressure ratio is computed by taking the exhaust pipe pressure losses Δp_{ep} into account as

$$\Pi_t = \frac{p_{\text{er}}}{p_{\text{amb}} + \Delta p_{\text{ep}}}, \tag{6.17}$$

where p_{er} is the pressure of the exhaust receiver. The temperature at the turbine outlet T_t^{out} can be computed from the turbine isentropic efficiency definition as

$$T_t^{out} = T_t^{in} \eta_t \left(1 - \Pi_t^{\frac{\gamma-1}{\gamma}} \right),$$
(6.18)

The rotational speed of the turbochargers ω_{tc} is a model state, defined by the power balance between compressor and turbocharger as

$$\frac{d\omega_{tc}}{dt} = \frac{P_t \eta_{tc}^{mech} - P_c}{J_{tc}\omega_{tc}},$$
(6.19)

where $P_t = \dot{m}_t \Delta h_t$, $P_c = \dot{m}_c \Delta h_c$ refer to the turbine and compressor power, respectively, with Δh_t, Δh_c being the enthalpy difference between the inlet and outlet of the turbine and compressor. J_{tc} refers to the turbocharger shaft inertia and η_{tc}^{mech} corresponds to the mechanical efficiency of the turbocharger unit, accounting for friction losses. J_{tc} and η_{tc}^{mech} are considered calibration parameters.

Cylinder—For the in-cylinder process, apart from the assumptions on the working medium described before, we have further neglected valve leakage and blow-by. Furthermore, the temperatures at the cylinder wall T_{cw}, head T_{hw}, piston wall T_{pw}, liner wall T_{lw}, exhaust valve wall T_{evw}, as well as the injected fuel temperature T_f are considered all uniform and constant. In fact, the temperature variations of the inner cylinder surface during the thermodynamic cycle are trivial compared to the temperature variations of the combustion gases (Descieux and Feidt 2007; Rakopoulos et al. 2004). Moreover, we have assumed a uniform cylinder pressure and that the combustion chamber volume consists of two zones. The burned zone contains incompletely oxidised fuel (denoted with the subscript b), whereas the unburned zone contains air and fuel (denoted with the subscript u). Each zone is spatially homogeneous, separated by a massless and infinitesimally thin flame, and no heat transfer takes place between the two zones. A schematic of the two combustion zone model is presented in Fig. 6.2. The main equations governing the two combustion zone model include the conservation of mass

$$\frac{dm}{d\theta} = \frac{dm_u}{d\theta} + \frac{dm_b}{d\theta} = \frac{dm_f}{d\theta} + \frac{dm_a}{d\theta}$$
(6.20)

where the subscripts u and b refer the the unburned and burned zone, respectively, and the subscripts a, f refer to air and fuel, respectively. The equations of state for the working medium in each zone can be described as

$$pV_u = m_u R_u T_u, \quad pV_b = m_b R_b T_b,$$
(6.21)

and the evolution of volume derivative with respect to crank angle in the two zones as

Fig. 6.2 Energy flow of the
two combustion zone model
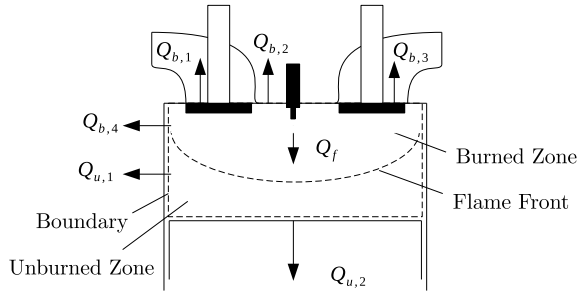
$$\frac{\mathrm{d}V}{\mathrm{d}\theta} = \frac{\mathrm{d}V_u}{\mathrm{d}\theta} + \frac{\mathrm{d}V_b}{\mathrm{d}\theta}, \tag{6.22}$$

in which the instantaneous cylinder volume can be expressed as a function of crank-angle θ according to the kinematics of the crankshaft as (Merker et al. 2005; Heywood 1988)

$$V(\theta) = V_c + B^2 \frac{\pi}{4}\left(l_r + a - s(\theta)\right), \quad s(\theta) = a + \cos\theta + \sqrt{l_r^2 - a^2 \sin\theta^2}, \tag{6.23}$$

where $V_c = V_s/(CR - 1)$ is the combustion chamber volume, V_s is the stroke volume, CR is the geometric compression ration, B is the bore diameter, l_r is the connecting rod length, and a is the crank radius.

Finally, the energy conservation equations for each combustion zone can be expressed as

$$\frac{\mathrm{d}(m_u u_u)}{\mathrm{d}\theta} = -p\frac{\mathrm{d}V_u}{\mathrm{d}\theta} - \sum_i \frac{\mathrm{d}Q_{u_i}}{\mathrm{d}\theta} - h_u \frac{\mathrm{d}m_b}{\mathrm{d}\theta} \tag{6.24}$$

$$\frac{\mathrm{d}(m_b u_b)}{\mathrm{d}\theta} = -p\frac{\mathrm{d}V_b}{\mathrm{d}\theta} - \sum_i \frac{\mathrm{d}Q_{b_i}}{\mathrm{d}\theta} + h_u \frac{\mathrm{d}m_b}{\mathrm{d}\theta} + \frac{\mathrm{d}Q_f}{\mathrm{d}\theta} \tag{6.25}$$

where $\sum_i \frac{\mathrm{d}Q_i}{\mathrm{d}\theta}$ for each one of the combustion zones refers to the summation of heat transfer rates through the engine's different parts surfaces in contact with the cylinder gases and $\frac{\mathrm{d}Q_f}{\mathrm{d}\theta}$ refers to the heat release rate.

Burn fraction and heat release rate in internal combustion engines are mostly governed by functions based on the law of Normal distribution of continuous random variables. In this context, one of the most popular functions is the Wiebe function (Ghojel 2010; Galindo et al. 2011). While the Wiebe function by no means describes the complex fuel air mixing in the diesel combustion process, it can provide valuable thermodynamic input for the model in terms of a realistic shape of the heat release. In this work, we have exploited a double-Wiebe profile for the premixed and diffusive combustion processes (Miyamoto et al. 1985; Kökkülünk et al. 2016) as reported in (Merker et al. 2005).

$$\frac{\mathrm{d}Q_{f,1}}{\mathrm{d}\theta} = Q_{f,1}\alpha(m_1 + 1)\left(\frac{\theta - \theta_{\mathrm{SOC}_1}}{\Delta\theta_{\mathrm{CD},1}}\right)^{m_1} \mathrm{e}^{-\alpha_i\left(\frac{\theta - \theta_{\mathrm{SOC}_1}}{\Delta\theta_{\mathrm{CD}_1}}\right)^{m_1+1}}, \tag{6.26}$$

$$\frac{\mathrm{d}Q_{f,2}}{\mathrm{d}\theta} = Q_{f,2}\alpha(m_2 + 1)\left(\frac{\theta - \theta_{\mathrm{SOC}_2}}{\Delta\theta_{\mathrm{CD},2}}\right)^{m_2} \mathrm{e}^{-\alpha_2\left(\frac{\theta - \theta_{\mathrm{SOC}_2}}{\Delta\theta_{\mathrm{CD}_2}}\right)^{m_2+1}}, \tag{6.27}$$

$$Q_{f,1} = q Q_{f,tot}, \quad Q_{f,2} = (1 - q)Q_{f,tot}, \quad \frac{\mathrm{d}Q_{f,\mathrm{tot}}}{\mathrm{d}\theta} = \frac{\mathrm{d}Q_{f,1}}{\mathrm{d}\theta} + \frac{\mathrm{d}Q_{f,2}}{\mathrm{d}\theta}, \tag{6.28}$$

where α is a factor related to the percentage of the total energy added with the fuel at the end of combustion $\eta_{\mathrm{conv,total}}$ as

$$\alpha = -\ln\left(1 - \eta_{\mathrm{conv,total}}\right), \tag{6.29}$$

its value is related to the combustion efficiency and it was assumed equal to 6.9 as suggested in Theotokatos et al. (2018) and Gogoi and Baruah (2010). Moreover, $Q_{f,tot} = m_f LHV_f$ represents the total thermal energy of the fuel released during combustion, q is the fraction of heat release of the first Wiebe profile, $\theta_{\mathrm{SOC},i}$ corresponds to the start of combustion, m_1 and m_2 are the Vibe form factors, and $\Delta\theta_{\mathrm{CD},i}$ denotes the combustion duration for each Wiebe profile. For the latter, the estimation of the ignition delay $\Delta\theta_{id}$ is required, for example according to Sitkei (1963) as

$$\Delta\theta_{id} = 6n_e 10^{-3}\left(a_{\mathrm{IGD}} + \left(p^{-0.7}b_{\mathrm{IGD}} + p^{-1.8}c_{\mathrm{IGD}}\right)\mathrm{e}^{\frac{7800}{6.9167RT}}1.0197\right), \tag{6.30}$$

where n_e is the engine rotational speed (expressed in Hz). The constants a_{IGD}, b_{IGD}, c_{IGD} are treated as calibration parameters.

In Eqs. (6.26) and (6.27), the constants m_1, m_2, $\Delta\theta_{\mathrm{CD}_1}$, and $\Delta\theta_{\mathrm{CD}_2}$ for each Wiebe profile are calibrated at the engine reference point (subscript ref) and updated for other operating points according to Woschni and Anisits (1973)

$$m = (m_{\mathrm{ref}} + \Delta m)\left(\frac{\theta_{\mathrm{IGD,ref}}}{\theta_{\mathrm{IGD}}}\right)^{a_{\mathrm{VM}}}\left(\frac{n_{e,\mathrm{ref}}}{n_e}\right)^{b_{\mathrm{VM}}}\left(\frac{p_{\mathrm{IVC}}}{p_{\mathrm{IVC,ref}}}\cdot\frac{V_{\mathrm{IVC}}}{V_{\mathrm{IVC,ref}}}\cdot\frac{T_{\mathrm{IVC,ref}}}{T_{\mathrm{IVC}}}\right)^{c_{\mathrm{VM}}} - \Delta_m, \tag{6.31}$$

$$\Delta\theta_{\mathrm{CD}} = \Delta\theta_{\mathrm{CD,ref}}\left(\frac{\lambda_{\mathrm{ref}}}{\lambda}\right)^{a_{\mathrm{CD}}}\left(\frac{n_e}{n_{e,\mathrm{ref}}}\right)^{b_{\mathrm{CD}}}, \tag{6.32}$$

The constants a_{CD}, b_{CD}, a_{VM}, b_{VM}, c_{VM} are regarded as calibration parameters, since their values are known to vary between engines of different types and sizes as reported in Merker et al. (2005). The subscripts IVC,ref and IVC refer to the inlet valve closing point at engine reference speeds $n_{e,\mathrm{ref}}$ and operating speed n_e, respectively.

The heat transfer between the mass trapped in the cylinder and the surrounding areas is calculated according to the standard Newtonian relation for convective heat transfer, as

$$\sum_i \frac{\mathrm{d}Q_{u_i}}{\mathrm{d}\theta} = k_{\mathrm{csa}}\sum_i A_i(T(\theta) - T_i), \tag{6.33}$$

Table 6.1 Coefficients for Woschni's heat transfer model of Eqs. (6.34), (6.35)

Phase	$c_1[-]$	$c_2[\text{m/s K}]$
Intake-exhaust	$6.18 + 0.417 c_c/c_m$	0
Compression	$2.28 + 0.308 c_c/c_m$	0
Combustion-expansion		$3.24 \cdot 10^{-3}$

with $i = \{\text{cw, hw, pw, lw, evw}\}$ referring to cylinder, head, piston, liner, and exhaust valve wall. The heat transfer coefficient k_{csa} is evaluated according to Woschni (1968), Merker et al. (2005)

$$k_{\text{csa}} = 127.93 p^{0.8} v^{0.8} B^{-0.2} T^{-0.53}, \tag{6.34}$$

where v is a representative velocity evaluated taking into account the mean piston speed $c_m = 2 L_s n_e$ (L_s is the stroke length), and the compression induced turbulence as Merker et al. (2005)

$$v = c_1 c_m + c_2 \frac{V_c T_{\text{IC}}}{p_{\text{IC}} V_{\text{IC}}} (p - p_0), \tag{6.35}$$

where p_0 is the cylinder pressure during motored operation, computed over a polytropic relation from the cylinder volume according to Merker et al. (2005). The constants c_1, c_2 are functions of the intake swirl c_c/c_m, according to Table 6.1. c_c/c_m is considered as a calibration parameter. The subscript IC refers to the cylinder conditions at the start of compression, when the intake valve closes.

We exploited the method of Chen and Flynn (1965) for the evaluation of the friction losses, according to which the friction mean effective pressure FMEP accounts for the effect of engine speed through a quadratic law. The effect of engine load is represented through the maximum in-cylinder pressure p_{max}, while the energy drawn by accessories and all the other invariable factors is accounted for by a constant term, as

$$\text{FMEP} = c_{f,1} + c_{f,2} p_{\text{max}} + c_{f,3} n_e + c_{f,4} n_e^2 \tag{6.36}$$

where coefficients $c_{f,1} - c_{f,4}$ are considered as calibration parameters.

The instantaneous cylinder torque is then computed by using the gross cylinder torque, through the cylinder indicated work, and cylinder torque due to friction. Since all cylinders are considered to operate under the same conditions, the brake power is computed using the current engine speed, multiplied by the cylinder torque and the number of cylinders in the engine.

The combustion products are evaluated exploiting the method of Rakopoulos et al. (1994), due to its minimal computational time requirements and reasonable agreement with experiments. For the burning zone, given its volume, temperature, mass of fuel burnt and mass of air entrained, the concentration of each species can be evaluated by solving a 11×11 non-linear system obtained from 7 non-linear equilibrium equations and 4 linear atom balance equations. This system is converted to a 4×4

non-linear system which can be solved efficiently by any root-finding algorithm [in this study, the Newton-Raphson method (Stoer and Bulirsch 2013)]. Finally, thermal NO has been evaluated according to the extended Zeldovich mechanism, for which the reaction rates were selected according to Hanson and Salimian (1984).

Equations (6.20)–(6.28) form a system of first order differential equations of the form $F(\theta, \mathbf{y}, \dot{\mathbf{y}}) = 0$ that is solved for each crank angle step by using the classic Runge-Kutta method (Stoer and Bulirsch 2013).

Sensor Dynamics—The thermal inertia of the temperature sensors which are mounted on the outer surface of the exhaust pipes, is modelled according to Llamas and Eriksson (2019) as

$$\frac{\mathrm{d}T_s}{\mathrm{d}t} = \frac{T - T_s}{\tau_s}, \tag{6.37}$$

where T_s refers to the temperature including the sensor dynamics, and T is the temperature of the working medium in the engine. The time constant τ_s is considered as a calibration parameter. Dynamic response for all other sensors has been neglected, as it is known to be in the order of milliseconds (Wahlström and Eriksson 2011).

Calculation Procedure—Inputs towards the cylinder model include the pressure, temperature, the medium composition from the scavenging manifold, the pressure of the exhaust manifold, engine rotational speed, and fuel injected per cycle from the governor. Subsequently, the cylinders air and exhaust gas mass flow rates, pressures, temperatures, the composition of the exhaust gas, and the equivalence ratio of the exhaust gas exiting the cylinders are calculated. Additional outputs include the energy flow of the exhaust gas exiting cylinders, the indicated power, the friction power, brake power torque, brake specific fuel consumption, and engine brake efficiency.

For all the other components (i.e., control volumes or flow elements) the following structure is employed. Inputs required for the flow elements are utilised from the adjacent flow receiver or fixed fluid structures for the engine boundaries which include the necessary parameters to fully characterise the working medium state (temperature, pressure, composition). Subsequently, mass and energy flows through the flow elements are computed and provided to the adjacent control volumes. In addition, the absorbed compressor torque and produced turbine torque are calculated and used as inputs to the turbocharger shaft element, which derives the turbocharger speed, which, in turn, is provided to the turbine and compressor blocks.

This framework forms an additional system of first order differential equations in the form $F(t, \mathbf{y}, \dot{\mathbf{y}}) = 0$, that is solved for each time step by using the classic Runge-Kutta method (Stoer and Bulirsch 2013). In total, the model contains 50 states over two major integration steps. Parameters include the geometric data of the engine, the intake and exhaust valves profiles, the compressor and turbine performance maps, the bypass valve geometric and control details, constants present in any sub-model, and the ambient conditions for the engine boundaries. Finally, initial values are also required for the engine and turbocharger rotational speeds, and the temperature, pressure and composition of the working medium contained in the scavenging and exhaust manifolds.

Model Parameterisation—The proposed model contains internal feedback systems, hence the modelling errors of any subsystems will be propagated and amplified towards the rest of the model. For instance, errors in the exhaust temperature will affect the turbine power production, which will in turn alter the scavenging pressure, and this finally will modify the exhaust temperature prediction anew. Due to this fact, balancing out the complete model by readjusting the model parameters is essential to obtain an overall accurate model (Llamas and Eriksson 2019).

The calibration process is treated as an optimisation problem, with the objective being to minimise the error between the model estimated outputs and the available measurements.

Formally, we seek the solution of the following continuous, non-convex problem

$$\arg\min_{\phi} \quad \hat{L}(\phi, \mathcal{D}_n) = \sum_{i=1}^{M} l(h(\boldsymbol{x}_i, \phi), \boldsymbol{y}_i), \tag{6.38}$$

$$\text{s.t.} \quad \phi_{\min} \leq \phi \leq \phi_{\max}$$

where h refers to the outputs of the PM, ϕ is the set of parameters that needs to be estimated from a given bounded space Φ, $\boldsymbol{x}_i$ refers to the measurements corresponding with the model inputs, and $\boldsymbol{y}_i$ refers to the measurements corresponding with the model outputs. $\hat{L}(\phi, \mathcal{D}_n)$ is the empirical error of the model h on the dataset $\mathcal{D}_n = \{(\boldsymbol{x}_1, \boldsymbol{y}_1), \ldots, (\boldsymbol{x}_n, \boldsymbol{y}_n)\}$, measured according to a loss function $\ell(h(\boldsymbol{x}, \boldsymbol{\theta}), \boldsymbol{y})$.

We have adopted the absolute relative error, given by

$$\ell\left(h\left(\boldsymbol{x}_i, \boldsymbol{\theta}\right), \boldsymbol{y}_i\right) = \sum_{j=1}^{S} \left| \frac{y_i^j - h^j(\boldsymbol{x}_i, \boldsymbol{\theta})}{y_i^j} \right| \tag{6.39}$$

Note that, because $\boldsymbol{y}$ is a vector, the loss function of Eq. (6.39) refers to the sum of relative errors of all model outputs $j = (1, \ldots, S)$ and their corresponding measured values.

Given the nature of the problem, a Derivative-Free Optimisation (DFO) method must be exploited, as obtaining or estimating the derivatives of the physical models with respect to the parameters is a computationally and time-intensive procedure. The literature on DFO methods is quite large, with a variety of algorithms that can solve different classes of problems (Conn et al. 2009; Galinier et al. 2013; Floudas and Pardalos 2008).

In this work, we leveraged an algorithm from the class of directional direct search methods: the Mesh-Adaptive Direct Search (MADS) algorithm, which is a local optimisation technique with established convergence theory under some mild assumptions (Audet and Dennis 2006; Audet et al. 2008). MADS is an extension of the Generalized Pattern Search algorithm (Torczon 1997; Lewis et al. 2000), specifically developed to handle non-smooth black-box problems. It is an iterative method that uses a discretisation of the solution space, called the mesh, to select and evaluate new trial points, given an initial iterate. Each iteration consists of two steps:

the search and the poll, followed by a parameter update step. If the search step succeeds (i.e., the selected trial point improves upon the current iterate), then this trial point becomes the new iterate and the poll step is skipped. If the search step fails, the poll step becomes mandatory. The poll is used to choose mesh points near the current iterate and to evaluate their objective and constraint values. If the poll fails to find a better solution, the update step will reduce the mesh size and the poll size, to concentrate near the current iterate. The mesh size is the parameter that scales the space discretization and the poll size is the maximum distance allowed between a trial point and the current iterate. On the other hand, once a better solution is found, the pol step terminates and the update step increases the mesh size. This process is repeated until a stopping condition is satisfied.

Given that our problem is highly non-linear and non-convex, there is no guarantee that the solution obtained corresponds to the global optima (Floudas and Pardalos 2008). In order to ensure the quality of the final solution the algorithm has been started from a number of different initial points, and from all solutions obtained, the best one has been chosen (Martí 2003).

The dynamic behaviour of the model is largely defined by the turbocharger inertias, the control volume sizes, and the time constants of the temperature sensors. The optimisation algorithm was initialised by a single starting point with suitable values of the turbocharger inertia corresponding to other engines of this size, whereas the values of the control volumes have been set to reasonable values based on the real pipe volume sizes from the engine design drawings.

6.3.2 Data Driven Models

In the proposed context of developing a fast yet accurate dynamic model of a four-stroke marine DE, a general modelisation framework can be defined, characterised by an input space $\mathcal{X} \subseteq \mathbb{R}^d$, an output space $\mathcal{Y} \subseteq \mathbb{R}^b$, and an unknown relation $\mu : \mathcal{X} \rightarrow \mathcal{Y}$ to be learned (Shalev-Shwartz and Ben-David 2014; Hamilton 2020). For what concerns this work, $\mathcal{X}$ is composed by the measurements available from the engine monitoring system (see Sect. 6.4), while the output space $\mathcal{Y}$ refers to the target features accounting for the engine fuel consumption, turbocharger rotational speed, turbine outlet temperature, and exhaust manifold temperature (see Sect. 6.4).

In this context, the authors define the model $h : \mathcal{X} \rightarrow \mathcal{Y}$ as an artificial simplification of μ. Analogously to what has been done in Sect. 6.3.1 we will assume to know all the information until time t_0 to make a prediction of the quantity of interest. In particular, we will consider all the information in $[t_0 - \Delta, t_0]$ (see Fig. 6.3). Δ represents how much history of the different available data we want to exploit to make predictions. Δ is an hyperparameter for which an optimal value exists: too much history (too large Δ) will make us face with the curse of dimensionality while too little history (too small Δ) will limit our ability to make accurate predictions (Shalev-Shwartz and Ben-David 2014; Oneto 2020; Hamilton 2020).
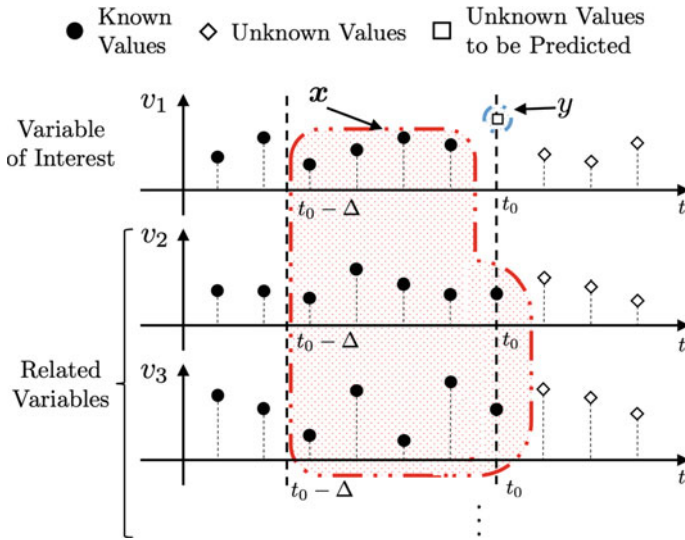
Fig. 6.3 Input and output variables of the DDMs

The model h, as described in Sect. 6.1 can be obtained with different kinds of techniques, for example, requiring some physical knowledge of the problem, as in PMs (see Sect. 6.3.1), or the acquisition of large amounts of data, as in DDMs or using both information (see Sect. 6.3.3). In this section we will use a state-of-the-art DDM. Between the DDMs it is possible to identify two families of approaches (Shalev-Shwartz and Ben-David 2014; Goodfellow et al. 2016). The first one, comprising traditional Machine Learning methods, needs an initial phase where the features must be defined a-priori from the data via feature engineering or implicit or explicit feature mapping (Shalev-Shwartz and Ben-David 2014; Zheng and Casari 2018; Shawe-Taylor and Cristianini 2004). The second family, which includes deep learning methods, automatically learns both the features and the models from the data (Goodfellow et al. 2016). For small cardinality datasets and outside particular applications (e.g., computer vision and natural language processing) Deep Learning does not perform well since they require huge amount of data to be reliable and to outperform traditional Machine Learning models (Fernández-Delgado et al. 2014; Wainberg et al. 2016).

In the Machine Learning maps the problem our problem can be easily mapped in a typical regression problem (Vapnik 1998; Shawe-Taylor and Cristianini 2004). In fact, ML techniques aim at estimating the unknown relationship μ between input and output through a learning algorithm $\mathscr{A}_{\mathcal{H}}$ which exploits some historical data to learn h and where $\mathcal{H}$ is a set of hyperparameters which characterises the generalisation performance of $\mathscr{A}$ (Oneto 2020). The historical data consists on a series of n examples of the input/output relation μ and are defined as $\mathcal{D}_n = \{(\boldsymbol{x}_1, y_1), \ldots, (\boldsymbol{x}_n, y_n)\}$ where $\boldsymbol{x} \in \mathcal{X}$ and $y \in \mathcal{Y}$.

In this paper we will leverage on a Machine Learning model coming from the Kernel Methods family called Kernel Regularised Least Squares (KRLS) (Vovk 2013). The idea behind KRLS can be summarised as follows. During the training phase, the quality of the learned function $h(\boldsymbol{x})$ is measured according to a loss function $\ell(h(\boldsymbol{x}), y)$ (Rosasco et al. 2004) with the empirical error

$$\hat{L}_n(h) = \frac{1}{n} \sum_{i=1}^{n} \ell(h(\boldsymbol{x}_i), y_i). \tag{6.40}$$

A simple criterion for selecting the final model during the training phase could then consist in simply choosing the approximating function that minimises the empirical error $\hat{L}_n(h)$. This approach is known as Empirical Risk Minimization (ERM) (Vapnik 1998). However, ERM is usually avoided in Machine Learning as it leads to severe overfitting of the model on the training dataset. As a matter of fact, in this case the training process could choose a model, complicated enough to perfectly describe all the training samples (including the noise, which afflicts them). In other words, ERM implies memorisation of data rather than learning from them. A more effective approach is to minimise a cost function where the trade-off between accuracy on the training data and a measure of the complexity of the selected model is achieved (Tikhonov and Arsenin 1979), implementing the Occam's razor principle

$$h^*: \min_{h} \quad \hat{L}_n(h) + \Lambda \, C(h). \tag{6.41}$$

In other words, the best approximating function h^* is chosen as the one that is complicated enough to learn from data without overfitting them. In particular, $C(\cdot)$ is a complexity measure: depending on the exploited Machine Learning approach, different measures are realised. Instead, $\Lambda \in [0, \infty)$ is a hyperparameter, that must be set a-priori and is not obtained as an output of the optimisation procedure: it regulates the trade-off between the overfitting tendency, related to the minimisation of the empirical error, and the underfitting tendency, related to the minimisation of $C(\cdot)$. The optimal value for Λ is problem-dependent, and tuning this hyperparameter is a non-trivial task, as will be discussed later in this section. In KRLS, models are defined as

$$h(\boldsymbol{x}) = \boldsymbol{w}^T \boldsymbol{\varphi}(\boldsymbol{x}), \tag{6.42}$$

where $\boldsymbol{\varphi}$ is an a-priori defined Feature Mapping (FM) (Shalev-Shwartz and Ben-David 2014) allowing to keep the structure of $h(\boldsymbol{x})$ linear. The complexity of the models, in KRLS, is measured as

$$C(h) = \|\boldsymbol{w}\|^2, \tag{6.43}$$

i.e., the Euclidean norm of the set of weights describing the regressor, which is a standard complexity measure in ML (Shalev-Shwartz and Ben-David 2014; Vovk

2013). Regarding the loss function, the square loss is typically adopted because of its convexity, smoothness, and statistical properties (Rosasco et al. 2004)

$$\hat{L}_n(h) = \frac{1}{n} \sum_{i=1}^{n} \ell(h(\boldsymbol{x}_i), y_i) = \frac{1}{n} \sum_{i=1}^{n} [h(\boldsymbol{x}_i) - y_i]^2 . \tag{6.44}$$

Consequently, Problem (6.41) can be reformulated as

$$\boldsymbol{w}^*: \min_{\boldsymbol{w}} \quad \sum_{i=1}^{n} \left[\boldsymbol{w}^T \boldsymbol{\varphi}(\boldsymbol{x}) - y_i \right]^2 + \Lambda \|\boldsymbol{w}\|^2. \tag{6.45}$$

By exploiting the Representer Theorem (Schölkopf et al. 2001), the solution h^* of the Problem (6.45) can be expressed as a linear combination of the samples projected in the space defined by $\boldsymbol{\varphi}$

$$h^*(\boldsymbol{x}) = \sum_{i=1}^{n} \iota_i \boldsymbol{\varphi}(\boldsymbol{x}_i)^T \boldsymbol{\varphi}(\boldsymbol{x}). \tag{6.46}$$

It is worth underlining that, according to the kernel trick, it is possible to reformulate $h^*(\boldsymbol{x})$ without an explicit knowledge of $\boldsymbol{\varphi}$, and consequently avoiding the curse of dimensionality of computing $\boldsymbol{\varphi}$, by using a proper kernel function $K(\boldsymbol{x}_i, \boldsymbol{x}) = \boldsymbol{\varphi}(\boldsymbol{x}_i)^T \boldsymbol{\varphi}(\boldsymbol{x})$

$$h^*(\boldsymbol{x}) = \sum_{i=1}^{n} \iota_i K(\boldsymbol{x}_i, \boldsymbol{x}). \tag{6.47}$$

Several kernel functions can be retrieved in literature (Scholkopf 2001; Cristianini and Shawe-Taylor 2000), each one with a particular property that can be exploited based on the problem under exam. Usually the Gaussian kernel is chosen

$$K(\boldsymbol{x}_i, \boldsymbol{x}) = e^{-\gamma \|\boldsymbol{x}_i - \boldsymbol{x}\|^2}, \tag{6.48}$$

because of the theoretical reasons described in Keerthi and Lin (2003), Oneto et al. (2015) and because of its effectiveness (Fernández-Delgado et al. 2014; Wainberg et al. 2016). γ is another hyperparameter, which regulates the nonlinearity of the solution that must be tuned as explained later. Basically the Gaussian kernel is able to implicitly create an infinite dimensional $\boldsymbol{\varphi}$ and thanks to this, the KRLS are able to learn any possible function (Keerthi and Lin 2003). The KRLS problem of Eq. (6.45) can be reformulated by exploiting kernels as

$$\iota^*: \min_{\iota} \quad \|Q\iota - y\|^2 + \Lambda \iota^T Q\iota, \tag{6.49}$$

where $y = [y_1, \ldots, y_n]^T$, $\iota = [\iota_1, \ldots, \iota_n]^T$, the matrix Q such that $Q_{i,j} = K(\boldsymbol{x}_j, \boldsymbol{x}_i)$, and the identity matrix $I \in \mathbb{R}^{n \times n}$. By setting the gradient equal to zero w.r.t. ι it is possible to state that

$$(Q + \Lambda I)\,\iota^* = y, \tag{6.50}$$

which is a linear system for which effective solvers have been developed over the years, allowing it to cope with even very large sets of training data (Young 2003).

The problems that still have to be faced is how to tune the hyperparameters of the approach (Λ, γ, and Δ^- for the second DT) and to estimate the performance of the final model. Model Selection (MS) and Error Estimation (EE) deal exactly with these problems (Oneto 2020). Resampling techniques are commonly used by researchers and practitioners since they work well in most situations and this is why we will exploit them in this work (Oneto 2020). Other alternatives exist, based on the Statistical Learning Theory, but they tend to underperform resampling techniques in practice (Oneto 2020). Resampling techniques are based on a simple idea: the original dataset $\mathcal{D}_n$ is resampled once or many (n_r) times, with or without replacement, to build three independent datasets called learning, validation and test sets, respectively $\mathcal{L}_l^r$, $\mathcal{V}_v^r$, and $\mathcal{T}_t^r$, with $r \in \{1, \ldots, n_r\}$ such that

$$\mathcal{L}_l^r \cap \mathcal{V}_v^r = \oslash, \quad \mathcal{L}_l^r \cap \mathcal{T}_t^r = \oslash, \quad \mathcal{V}_v^r \cap \mathcal{T}_t^r = \oslash, \quad \mathcal{L}_l^r \cup \mathcal{V}_v^r \cup \mathcal{T}_t^r = \mathcal{D}_n. \tag{6.51}$$

Subsequently, to select the best hyperparameters' combination $\mathcal{H} = \{\Lambda, \gamma, (\Delta^-)\}$ in a set of possible ones $\mathfrak{H} = \{\mathcal{H}_1, \mathcal{H}_2, \ldots\}$ for the algorithm $\mathscr{A}_{\mathcal{H}}$ or, in other words, to perform the MS phase, the following procedure has to be applied:

$$\mathcal{H}^*: \arg\min_{\mathcal{H} \in \mathfrak{H}} \sum_{r=1}^{n_r} M(\mathscr{A}_{\mathcal{H}}(\mathcal{L}_l^r), \mathcal{V}_v^r), \tag{6.52}$$

where $h = \mathscr{A}_{\mathcal{H}}(\mathcal{L}_l^r)$ is a model built with the algorithm $\mathscr{A}$ with its set of hyperparameters $\mathcal{H}$ and with the data $\mathcal{L}_l^r$, and where $M(h, \mathcal{V}_v^r)$ is a desired metric. Since the data in $\mathcal{L}_l^r$ are independent from the data in $\mathcal{V}_v^r$, $\mathcal{H}^*$ should be the set of hyperparameters which allows achieving a small error on a data set that is independent from the training set. Then, to evaluate the performance of the optimal model which is $h_{\mathscr{A}}^* = \mathscr{A}_{\mathcal{H}^*}(\mathcal{D}_n)$ or, in other words, to perform the EE phase, the following procedure has to be applied:

$$M(h_{\mathscr{A}}^*) = \frac{1}{n_r} \sum_{r=1}^{n_r} M(\mathscr{A}_{\mathcal{H}^*}(\mathcal{L}_l^r \cup \mathcal{V}_v^r), \mathcal{T}_t^r). \tag{6.53}$$

Since the data in $\mathcal{L}_l^r \cup \mathcal{V}_v^r$ are independent from the ones in $\mathcal{T}_t^r$, $M(f_{\mathscr{A}}^*)$ is an unbiased estimator of the true performance, measured with the metric M, of the final model (Oneto 2020). In this work we will rely on Complete k-fold cross validation which means setting $n_r \leq \binom{n}{k}\binom{n - \frac{n}{k}}{k}$, $l = (k-2)\frac{n}{k}$, $v = \frac{n}{k}$, and $t = \frac{n}{k}$ and the resam-

pling must be done without replacement (Oneto 2020). Note that, in our application, we have a further constraint in terms of dependence in time between the samples. For this reason, when resampling the data form $\mathcal{D}_n$ we actually keep data of different periods in $\mathcal{L}_l^r$, $\mathcal{V}_v^r$, and $\mathcal{T}_t^r$ (Hamilton 2020).

For what concerns the metric M that we will use in our paper we will rely on the Mean Absolute Error (MAE), the Mean Absolute Percentage of Error (MAPE) and the Pearson Product-Moment Correlation Coefficient PPMCC (Willmott and Matsuura 2005). Since in regression it is quite hard to synthesise the quality of a predictor in a single metric we will also rely on visualisation techniques like the scatter plot and histograms (Shao et al. 2017).

6.3.3 Hybrid Models

In this section we would like to depict a framework able to take into account both the physical knowledge about the problem encapsulated in the PMs of Sect. 6.3.1 and the information hidden in the available data as the DDMs of Sect. 6.3.2, into account. For this purpose authors will start from a simple observation: a HM, based on the previous observation, should be able to learn from the data without being too different, or too far away, from the PM.

From the Data Science and Machine Learning point of view, this requirement can be straightforwardly mapped in a typical ML Multi Task Learning (MTL) problem (Baxter 2000; Caruana 1997; Evgeniou and Pontil 2004; Bakker and Heskes 2003; Argyriou et al. 2008). MTL aims at simultaneously learning two concepts, in this case the PM and the available data, through a learning algorithm $\mathscr{A}_{\mathcal{H}}$ which exploits the data in $\mathcal{D}_n$ to learn a function h which is both close to the observation, the data $\mathcal{D}_n$ and the PM, namely its forecasts.

Consequently, in this case a slightly different scenario is presented where the dataset is composed by a triple of points $\mathcal{D}_n = \{(\boldsymbol{x}_1, y_1, p_1), \ldots, (\boldsymbol{x}_n, y_n, p_n)\}$ where p_i is the output of the PM in the point $\boldsymbol{x}_n$ with $i \in \{1, \ldots, n\}$. The target is to learn a function able to approximate both μ, namely the relation between the input $\boldsymbol{x} \in \mathcal{X}$ and the output $y \in \mathcal{Y}$, and the PM, namely the relation between the input and the output of the PM. Two tasks have to be learned. For this purpose there are two main approaches: the first approach is called Shared Task Learning (STL) and the second Independent Task Learning (ITL). While the latter independently learns a different model for each task, the former aims to learn a model that is common between all tasks. A well-known weakness of these methods is that they tend to generalise poorly on one of the two tasks (Baxter 2000). In this work, authors show that an appealing approach to overcome such limitations is provided by MTL (Baxter 2000; Caruana 1997; Evgeniou and Pontil 2004; Bakker and Heskes 2003; Argyriou et al. 2008). This methodology leverages on the information between the tasks to learn more accurate models.

In order to apply the MTL approach to this case, it is possible to modify the KRLS problem of Eq. (6.45) to simultaneously learn a shared model and a task

specific model which should be close to the shared model. In this way, authors obtain a model which is able to simultaneously learn the two tasks. The model that authors are interested in is the shared model, while the task specific models are just used as a tool. A shared model is defined as

$$h(\boldsymbol{x}) = \boldsymbol{w}^T \boldsymbol{\varphi}(\boldsymbol{x}), \tag{6.54}$$

and two task specific models as

$$h_i(\boldsymbol{x}) = \boldsymbol{w}_i^T \boldsymbol{\varphi}(\boldsymbol{x}), \quad i \in \{y, p\}. \tag{6.55}$$

Then, it is possible to state the MTL version of Eq. (6.45), as follows

$$\boldsymbol{w}^*, \boldsymbol{w}_y^*, \boldsymbol{w}_p^* : \min_{\boldsymbol{w}, \boldsymbol{w}_y, \boldsymbol{w}_p} \quad \sum_{i=1}^n \left[\boldsymbol{w}^T \boldsymbol{\varphi}(\boldsymbol{x}) - y_i \right]^2 + \left[\boldsymbol{w}^T \boldsymbol{\varphi}(\boldsymbol{x}) - p_i \right]^2$$
$$+ \sum_{i=1}^n \left[\boldsymbol{w}_y^T \boldsymbol{\varphi}(\boldsymbol{x}) - y_i \right]^2 + \left[\boldsymbol{w}_p^T \boldsymbol{\varphi}(\boldsymbol{x}) - p_i \right]^2$$
$$+ \Lambda \|\boldsymbol{w}\|^2 + \varkappa (\|\boldsymbol{w} - \boldsymbol{w}_y\|^2 + \|\boldsymbol{w} - \boldsymbol{w}_p\|^2), \tag{6.56}$$

where Λ is the usual regularization of KRLS and $\varkappa \in [0, \infty)$, instead, is another hyperparameter that forces the shared model to be close to the task specific models. Basically the MTL problem of Eq. (6.56) is a concatenation of three learning problems solved with KRLS plus a term which tries to keep a relation between all the three different problems.

By exploiting the kernel trick as in KRLS, it is possible to reformulate Problem (6.56), as follows

$$\boldsymbol{\iota}^*: \min_{\boldsymbol{\iota}} \quad \left\| \begin{bmatrix} Q & Q & 0 & 0 \\ Q & Q & 0 & 0 \\ 0 & 0 & Q & 0 \\ 0 & 0 & 0 & Q \end{bmatrix} \boldsymbol{\iota} - \begin{bmatrix} \boldsymbol{y} \\ \boldsymbol{p} \\ \boldsymbol{y} \\ \boldsymbol{p} \end{bmatrix} \right\|^2$$
$$+ \boldsymbol{\iota}^T \begin{bmatrix} (\Lambda + 2\varkappa)Q & (\Lambda + 2\varkappa)Q & -\varkappa Q & -\varkappa Q \\ (\Lambda + 2\varkappa)Q & (\Lambda + 2\varkappa)Q & -\varkappa Q & -\varkappa Q \\ -\varkappa Q & -\varkappa Q & \varkappa Q & 0 \\ -\varkappa Q & -\varkappa Q & 0 & \varkappa Q \end{bmatrix} \boldsymbol{\iota}, \tag{6.57}$$

where $\boldsymbol{p} = [p_1, \ldots, p_n]^T$. The solution of this problem is again equivalent to solving a linear system

$$
\begin{bmatrix}
Q + (\Lambda + 2\varkappa)I & Q + (\Lambda + 2\varkappa)I & -\varkappa I & -\varkappa I \\
Q + (\Lambda + 2\varkappa)I & Q + (\Lambda + 2\varkappa)I & -\varkappa I & -\varkappa I \\
-\varkappa I & -\varkappa I & Q + \varkappa I & 0 \\
-\varkappa I & -\varkappa I & 0 & Q + \varkappa I
\end{bmatrix}
\boldsymbol{\iota}^* =
\begin{bmatrix}
\boldsymbol{y} \\
\boldsymbol{p} \\
\boldsymbol{y} \\
\boldsymbol{p}
\end{bmatrix}. \tag{6.58}
$$

The function that the authors are interested in, the shared one, can be expressed as follows

$$
h(\boldsymbol{x}) = \boldsymbol{w}^T \boldsymbol{\varphi}(\boldsymbol{x}) = \sum_{i=1}^{n} (\iota_i + \iota_{i+n}) K(\boldsymbol{x}_i, \boldsymbol{x}). \tag{6.59}
$$

What changes here, with respect to the MS phase of the DDM described in Sect. 6.3.2, is the MS phase where just Λ, γ, and also $\varkappa$ need to be tuned.

6.4 Case Study and Dataset Description

In this work, as a case study, we have exploited data acquired from a naval vessel equipped with a MAN B&W V28-33D medium speed four-stroke DE. The engine has 12 cylinders with 0.28m bore and 0.33m stroke, with a Maximum Continuous Rating (MCR) of 5.4MW at 1000rpm and two turbochargers (TCs) operating in parallel to deliver the necessary air. The main characteristics of the engine are summarised in Table 6.2.

The engine is characterised by a power-to-weight and power-to-installation space ratios favourable to fast mono-hull and multi-hull vessels, offshore patrol vessels with either single or twin engine-gear-propeller systems or corvettes, frigates and destroyers with combined propulsion plant configurations, such as COmbined Diesel

Table 6.2 Main characteristics of the MAN 12 V28-33D engine

Feature	Value	Unit
Cylinders	V12, 16, 20	[–]
Bore diameter	280	[mm]
Stroke length	330	[mm]
Number of cylinders	12	[–]
Revolutions per cycle	2	[–]
Engine speed at MCR	1000	[rpm]
Brake power at 60% MCR	3240	[kW]
Brake power at 80% MCR	4320	[kW]
Brake power at MCR	5400	[kW]
Mean effective pressure	26.9	[bar]
Mean piston speed	11	[m/s]
Specific fuel consumption (100% load)	191	[g/kWh]
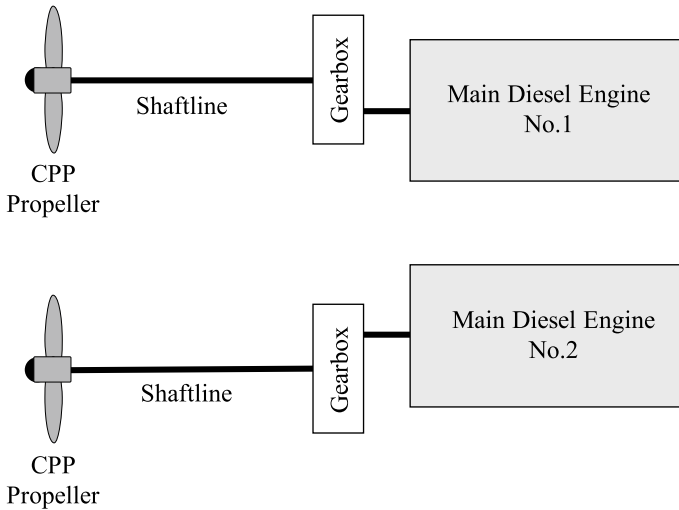
Fig. 6.4 Propulsion system layout for the holland class oceangoing patrol vessels

And Diesel (CODAD), COmbined Diesel Or Gas (CODOG), and COmbined Diesel And Gas (CODAG). The DE under investigation is installed on board one of the the Holland Class Oceangoing Patrol Vessels. The propulsion system of the vessel consists of two shafts with Controllable Pitch Propellers (CPP), a gearbox, and one DE per shaft, as shown in Fig. 6.4. This configuration is typical for multi-function ships that require silent, manoeuvrable, highly reliable and low emission propulsion.

The Patrol vessel is equipped with a data logging system which is used by the Royal Netherlands Navy both for on-board monitoring and control and for land-based performance analysis. The dataset utilised consists of two different data sources: standard measurements (steady-state) performed during Shop Trials (ST) that have been exploited to calibrate the PM model (see Sect. 6.3.1), and operational data originating from the vessel's data logging system, used by the ship operator for performance monitoring purposes, which has been exploited to evaluate the performance of the PM model in dynamic conditions (see Sect. 6.3.1), and to train, validate, and test the DDMs and HMs (see Sects. 6.3.2 and 6.3.3). Operational measurements are sampled at 3Hz for approximately 3 calendar years for a total of 7900 h of operations. A summary of the available measurements is reported in Table 6.3.

It should be noted that fuel consumption is measured using a mass flow meter which is known to be more accurate of the more common volume flow meters as it eliminates uncertainty on fuel density. However, measurements of fuel specific energy content are not available. Unfortunately, the energy content of a compound fuel can vary in quality among markets, a variation which is known to be in the order of ± 2 MJ/kg, or approximately $\pm 5\%$ (Coraddu et al. 2017). Moreover, measurements regarding the ambient conditions of the engine's surrounding environment are also not available, as well as the uncertainty of the measurements performed during the ST.

Table 6.3 Measurements available from the engine monitoring system

Variable name	Symbol	Unit
Time stamp	t	[hh:mm:ss]
Governor position	G_p	[–]
Engine rotational speed	n_e	[rpm]
Engine torque	M_e	[kNm]
Charge air temperature at scavenging receiver	T_{sc}	[°C]
Charge air temperature at compressor outlet	$T_{c,out}$	[°C]
Charge air temperature at compressor inlet	$T_{c,in}$	[°C]
Exhaust gas temperature at turbine outlet	$T_{t,out}$	[°C]
Main bearing no. 1 temperature	$T_{b,1}$	[°C]
Main bearing no. 2 temperature	$T_{b,2}$	[°C]
Main bearing no. 3 temperature	$T_{b,3}$	[°C]
Main bearing no. 4 temperature	$T_{b,4}$	[°C]
Main bearing no. 5 temperature	$T_{b,5}$	[°C]
Main bearing no. 6 temperature	$T_{b,6}$	[°C]
Main bearing no. 7 temperature	$T_{b,7}$	[°C]
Lube oil compartment no. 1 temperature	$T_{l,1}$	[°C]
Lube oil compartment no. 2 temperature	$T_{l,2}$	[°C]
Lube oil compartment no. 3 temperature	$T_{l,3}$	[°C]
Lube oil compartment no. 4 lube oil temperature	$T_{l,4}$	[°C]
Lube oil compartment no. 5 lube oil temperature	$T_{l,5}$	[°C]
Lube oil engine inlet temperature	$T_{le,in}$	[°C]
Lube oil engine outlet temperature	$T_{le,out}$	[°C]
High-temperature sea cooling water—inlet	$T_{ht,in}$	[°C]
High-temperature sea cooling water—outlet	$T_{ht,out}$	[°C]
Low-temperature sea cooling water—inlet	$T_{lt,in}$	[°C]
Low-temperature sea cooling water—outlet	$T_{lt,out}$	[°C]
Fuel oil supply temperature	T_f	[°C]
Charge air temperature at compressor outlet—bank A	$T_{c,out}^A$	[°C]
Charge air temperature at compressor outlet—bank B	$T_{c,out}^B$	[°C]
Charge air temperature at compressor inlet—bank A	$T_{c,in}^A$	[°C]
Charge air temperature at compressor inlet—bank B	$T_{c,in}^B$	[°C]
Charge air engine inlet pressure	$p_{ca,in}$	[Pa]
Charge air engine inlet temperature	$T_{ca,in}$	[°C]
Fuel consumption	$\dot{m}_f$	[kg/h]
TC rotational speed	N_{tc}	[rpm]
Turbine outlet temperature	$T_{t,out}$	[°C]
Exhaust receiver temperature	T_{er}	[°C]

6.5 Experimental Results

In this section, we exploited the data described in Sect. 6.4 to test the models developed in Sect. 6.3. To begin with, calibration results of the PM described in Sect. 6.5.1 are reported. Then a comparison of the performance of PMs, DDMs, and HMs in operational dynamic conditions is reported.

6.5.1 Zero Dimensional Diesel Engine Model Calibration Results

The PM model validation has been carried out taking into account both the standard (steady-state) measurements performed during ST and Stationary Operations (SO). To identify SO, the dataset was first split into a set of time intervals of continuous operation. Within each interval, operation under stationary conditions is defined as any continuous set of measurements for which the rotational speed and load of the engine vary by less than 1%, for a period of at least 3 hours. For each of these stationary conditions, the last 10 minutes of measurements were extracted and the median value of each signal was computed. This allowed us to summarise each stationary operation as one value per signal, for a total of 256 stationary operation points.

To perform the calibration and validation of the PM we exploited a subset of the data reported in Table 6.3. In particular, Table 6.4 reports the subset of the data source exploited as input, as validation on ST and SO, and comparison with the DDM and HM in transient analysis.

The performance metrics discussed in Sect. 6.3.2 are reported in Table 6.5 on the ST dataset.

The reported performances indicate that the model can capture all measurements well within 1% for engine loads ranging between 20 and 100%. The maximum combustion pressure shows the highest errors, with a MAPE equal to 0.98%. The lowest discrepancy between the PM and the measurements is reported for the temperature at the turbine outlet, with a MAPE of only 0.01%, well within the uncertainty of most conventional thermocouples used for this application. The prediction accuracy for all other variables is equally good regardless of the subsystem considered.

Regarding the validation of the model in SO, we have to consider that the performance of the PM have been assesses on a dataset representing the behaviour of the engine during sailing. Unfortunately, a holistic comparison on the performance of the PM on the ST and SO dataset is not possible as only a subset of signals is available for this second validation as reported in Table 6.6.

Nevertheless, the metrics reported in Table 6.6 reveal that the PM is still able to capture the performances of the DE in real operations. In fact, the MAPE on the compressor outlet temperature has increased from 0.638% on the ST to 2.752% on SO. Similarly, the scavenging manifold and turbine outlet temperatures have increased

Table 6.4 Subset of data source from Table 6.3 exploited as PM inputs, validation on ST and SO, and comparison with the DDM and HM in transient analysis
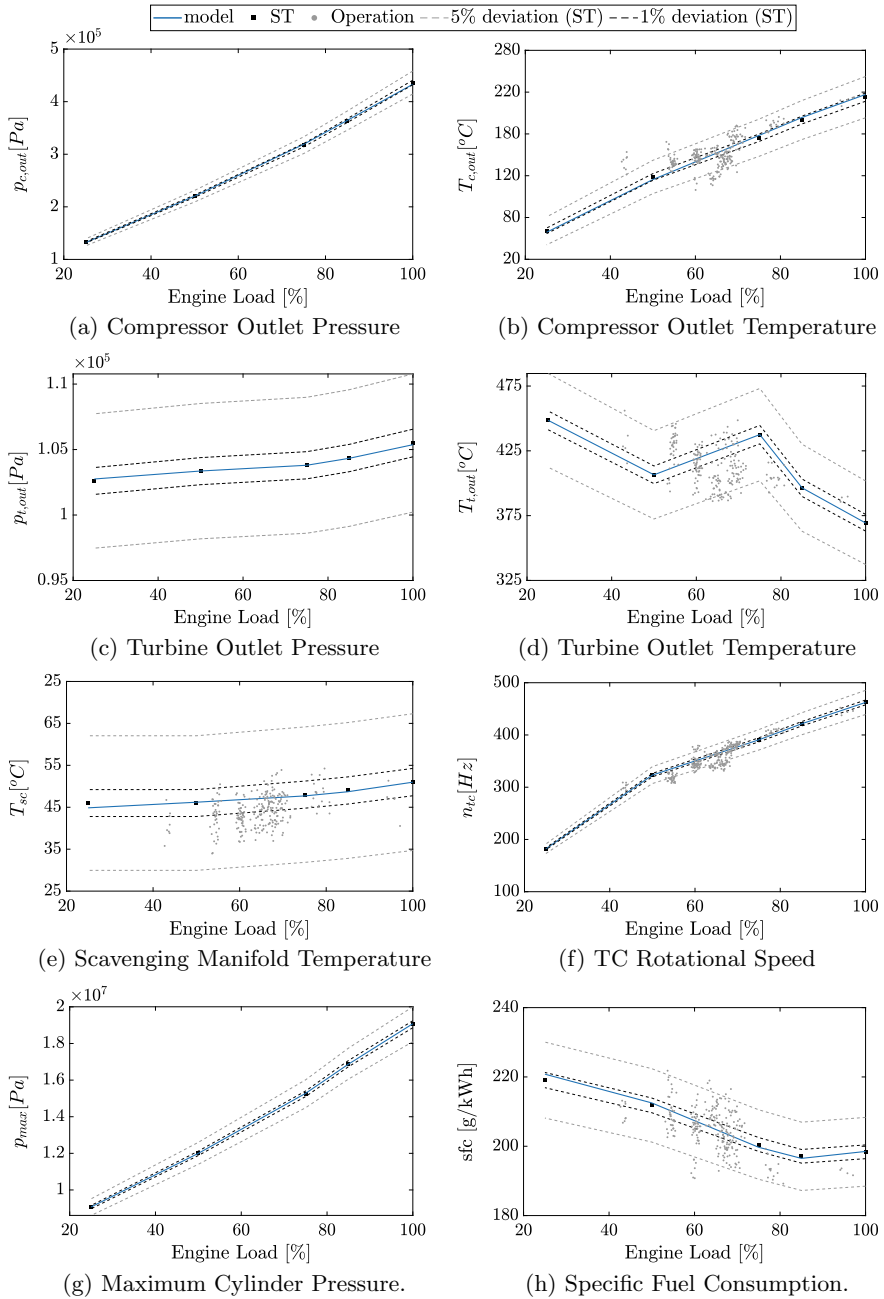
	Variable name	Symbol	Unit
Input	Engine rotational speed	n_e	[rpm]
	Governor position	G_p	[rpm]
Output for ST and SO validation	Compressor outlet pressure	$p_{c,\text{out}}$	[Pa]
	Compressor outlet temperature	$T_{c,\text{out}}$	[kg/h]
	Turbine outlet pressure	$p_{t,\text{out}}$	[Pa]
	Turbine outlet temperature	$T_{t,\text{out}}$	[°C]
	Scavenging receiver temperature	T_{sc}	[°C]
	TC Rotational speed	n_{tc}	[Hz]
	Maximum cylinder pressure	p_{max}	[Pa]
	Specific fuel consumption	sfc	[g/kWh]
Output for transient analysis	Fuel consumption	$\dot{m}_f$	[kg/h]
	TC rotational speed	N_{tc}	[Hz]
	Turbine outlet temperature	$T_{t,\text{out}}$	[°C]
	Exhaust receiver temperature	T_{er}	[°C]

Table 6.5 PM Performance metrics on the ST

Variable name	Symbol	Unit	MAE	MAPE [%]	PPMCC
Compressor outlet pressure	$p_{c,\text{out}}$	[Pa]	$1.2 \cdot 10^3$	0.363	1.000
Compressor outlet temperature	$T_{c,\text{out}}$	[K]	2.750	0.638	1.000
Turbine outlet pressure	$p_{t,\text{out}}$	[Pa]	62.354	0.060	1.000
Turbine outlet temperature	$T_{t,\text{out}}$	[K]	0.066	0.010	1.000
Scavenging manifold temperature	$T_{s,\text{in}}$	[K]	0.393	0.122	0.979
Turbocharger rotational speed	n_{tc}	[Hz]	4.302	0.041	0.989
Cylinder maximum pressure	p_{max}	[Pa]	$1.1 \cdot 10^5$	0.981	0.999
Specific fuel consumption	sfc	[g/kWh]	1.207	0.056	0.988

Table 6.6 Performance metrics on PM-SO dataset

Variable name	Symbol	Unit	MAE	MAPE [%]	PPMCC
Compressor outlet temperature	$T_{c,out}$	[K]	11.545	2.752	0.643
Turbine outlet temperature	$T_{t,out}$	[K]	3.798	1.199	0.342
Scavenging manifold temperature	$T_{sc,in}$	[K]	17.545	2.570	−0.145
Turbocharger rotational speed	n_{tc}	[Hz]	12.013	3.506	0.881
Specific fuel consumption	sfc	[g/kWh]	4.400	2.178	0.514

(a) Compressor Outlet Pressure

(b) Compressor Outlet Temperature

(c) Turbine Outlet Pressure

(d) Turbine Outlet Temperature

(e) Scavenging Manifold Temperature

(f) TC Rotational Speed

(g) Maximum Cylinder Pressure.

(h) Specific Fuel Consumption.

Fig. 6.5 PM verification in steady-state conditions (ST and SO)

Table 6.7 Subset of data source from Table 6.3 exploited as inputs and outputs of the DDM and HM

	Symbol					
Input variables for DDMs and HMs	n_e	$T_{l,4}$	T_{sc}	$T_{l,5}$	$T_{c,out}$	$T_{le,in}$
	$T_{c,in}$	$T_{le,out}$	$T_{t,out}$	$T_{ht,in}$	$T_{b,1}$	$T_{ht,out}$
	$T_{b,2}$	$T_{lt,in}$	$T_{b,3}$	$T_{lt,out}$	$T_{b,4}$	T_f
	$T_{b,5}$	$T_{c,out}^A$	$T_{b,6}$	$T_{c,out}^B$	$T_{b,7}$	$T_{c,in}^A$
	$T_{l,1}$	$T_{c,in}^B$	$T_{l,2}$	$p_{ca,in}$	$T_{l,3}$	$T_{ca,in}$
Output variables for DDMs and HMs	$\dot{m}_f$					
	N_{tc}					
	$T_{t,out}$					
	T_{er}					

from 0.122 and 0.01% to 1.2 and 2.6%, respectively. Moreover, a similar decrease in prediction capability can be observed for the specific fuel consumption and turbocharger rotational speed, with the MAPEs increasing from 0.041 and 0.056% to 3.5 and 2.2%, respectively. Finally, a visual impression of the results reported in Tables 6.5 and 6.6 is reported in Fig. 6.5 for various engine loading conditions.

6.5.2 Physical Model, Data Driven Model, and Hybrid Model

This section is devoted to the comparison between the PM, DDM, and HM. As a first step we have to detail the inputs and the outputs of the DDM and HM. For this purpose Table 6.7 reports the subset of Table 6.3 exploited ad inputs and outputs of the DDM and HM.

Then we have to report the hyperparametes ranges for the DDM and HM. For the DDM the set of hyperparameters tuned during the MS phase are $\mathcal{H} = \{\gamma, \Lambda\}$ chosen in $\mathfrak{H} = \{10^{-4.0}, 10^{-3.8}, \ldots, 10^{+4.0}\} \times \{10^{-4.0}, 10^{-3.8}, \ldots, 10^{+4.0}\}$. For the DDM the set of hyperparameters tuned during the MS phase are $\mathcal{H} = \{\gamma, \Lambda, \varkappa\}$ chosen in $\mathfrak{H} = \{10^{-4.0}, 10^{-3.8}, \ldots, 10^{+4.0}\} \times \{10^{-4.0}, 10^{-3.8}, \ldots, 10^{+4.0}\} \times \{10^{-4.0}, 10^{-3.8}, \ldots, 10^{+4.0}\}$.

All the tests have been repeated 30 times, and the average results are reported together with their t-student 95% confidence interval, to ensure the statistical validity of the results.

Table 6.8 reports the performance (measured with the MAE, MAPE, and PPMCC) of the different models (PM, DDM, and HM) for different values of $\Delta \in \{0, 10, 20, 30\}$ for the different targets to to predict ($\dot{m}_f$, N_{tc}, $T_{t,out}$, and T_{er}). Note that $\Delta = 0$ means that the authors do not exploit time series information from the past, for $\Delta > 0$ there is no PM result. Moreover, to improve the readability and better understand the quality of the results, Figs. 6.6, 6.7, 6.8 and 6.9 reports for $\Delta = 0$ the scatter
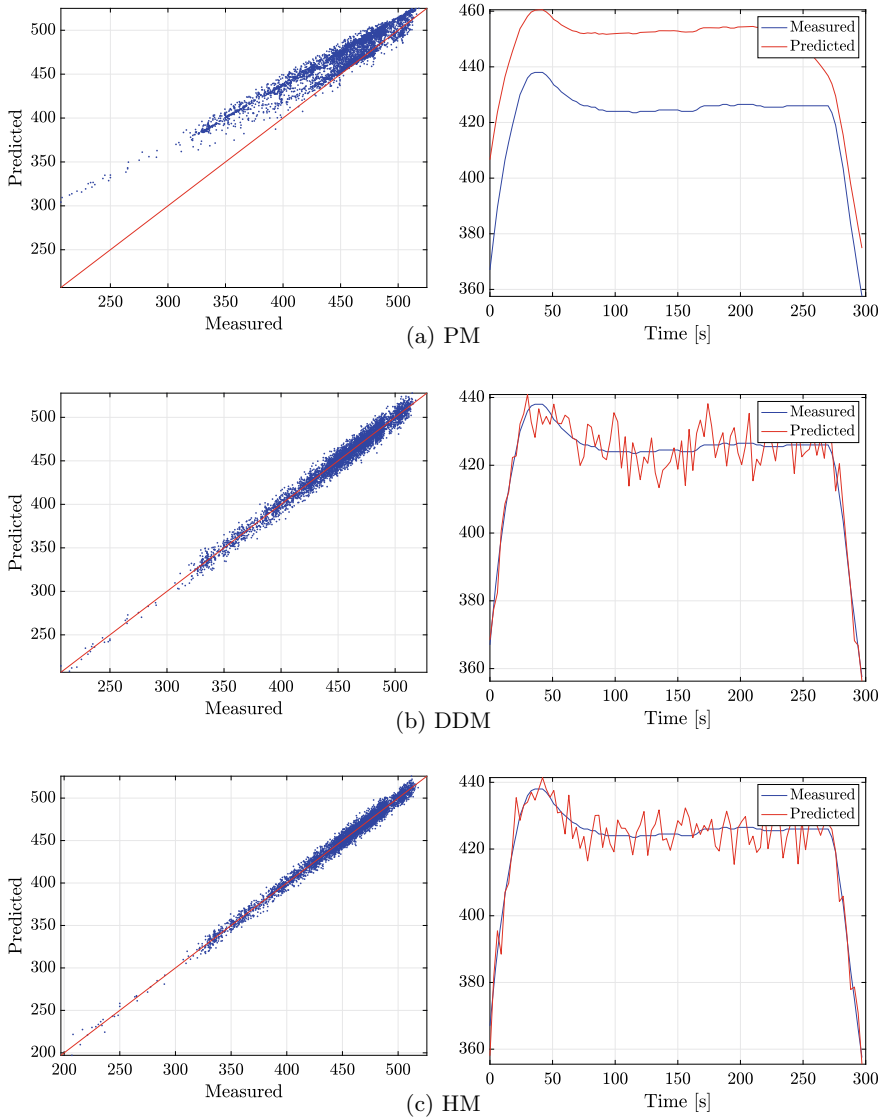
(a) PM

(b) DDM

(c) HM
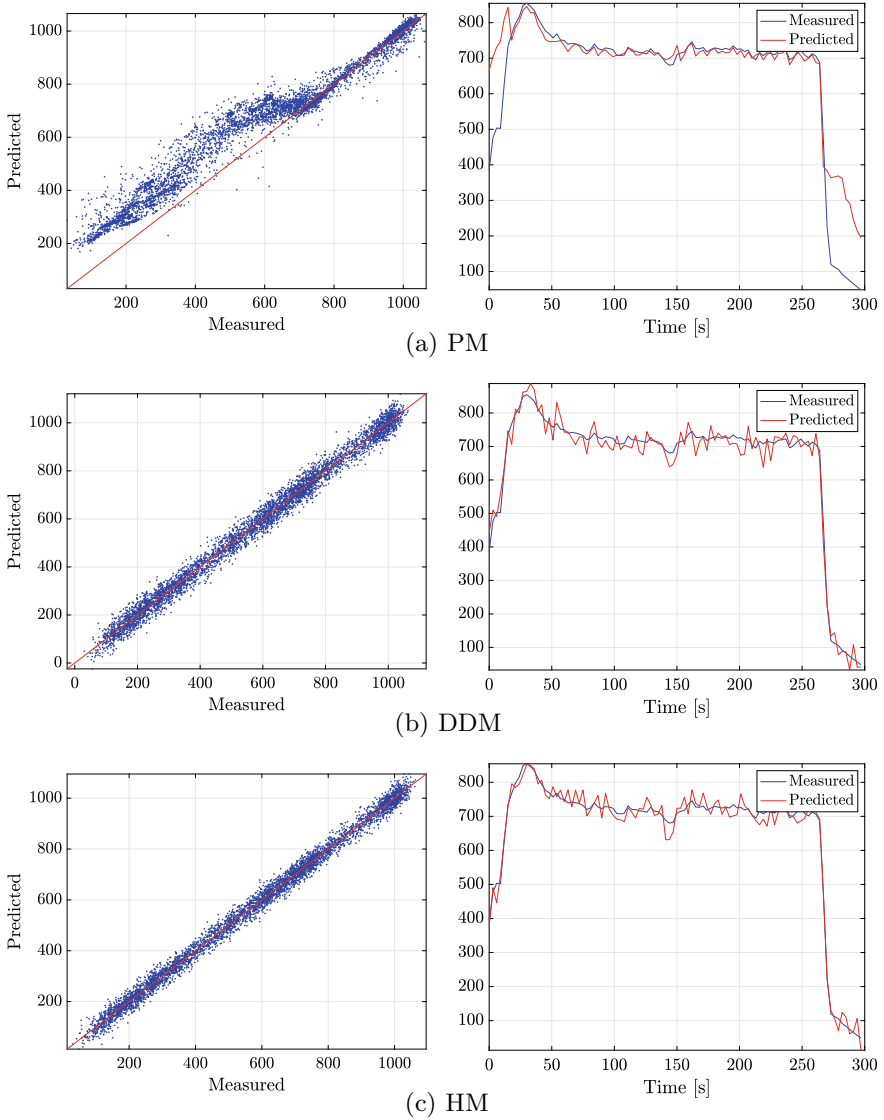
Fig. 6.6 Scatter plot (measured vs. predicted) and trend in time for the $\dot{m}_f$ (kg/h) output feature using the different models (PMs, DDMs, and HMs) with $\Delta = 0$
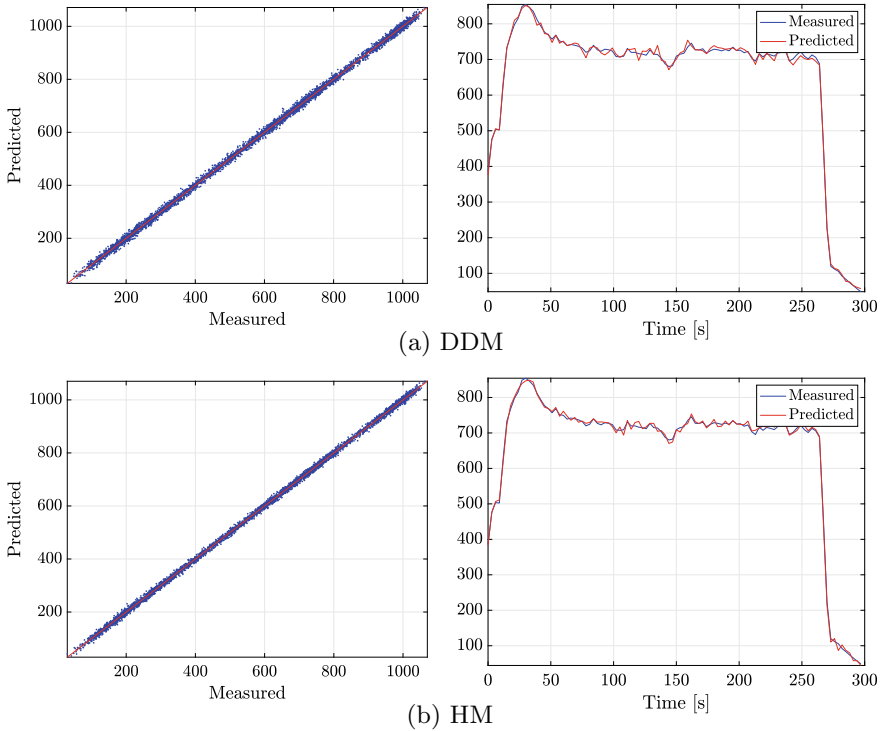
(a) PM

(b) DDM

(c) HM
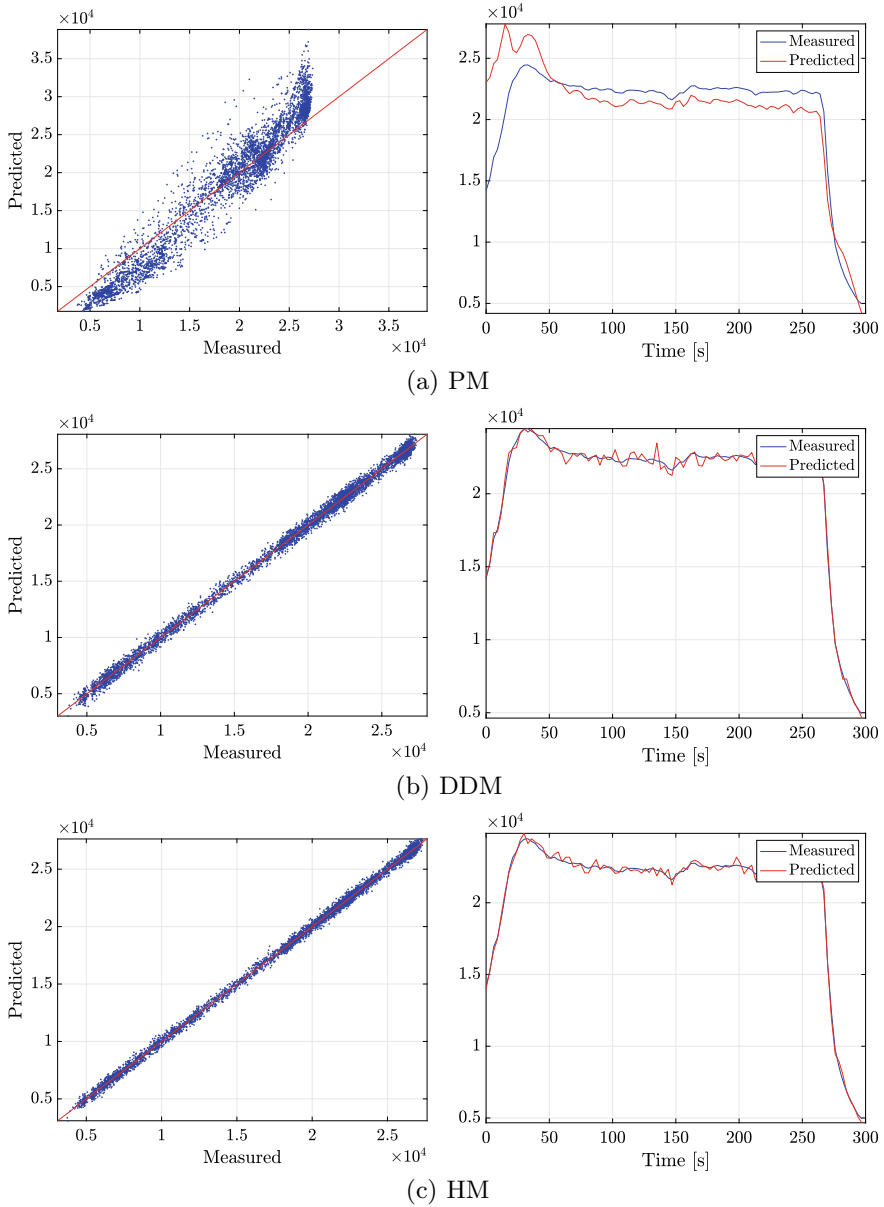
Fig. 6.7 Scatter plot (measured vs. predicted) and trend in time for the N_{tc} (rpm) output feature using the different models (PMs, DDMs, and HMs) with $\Delta = 0$

(a) PM

(b) DDM

(c) HM
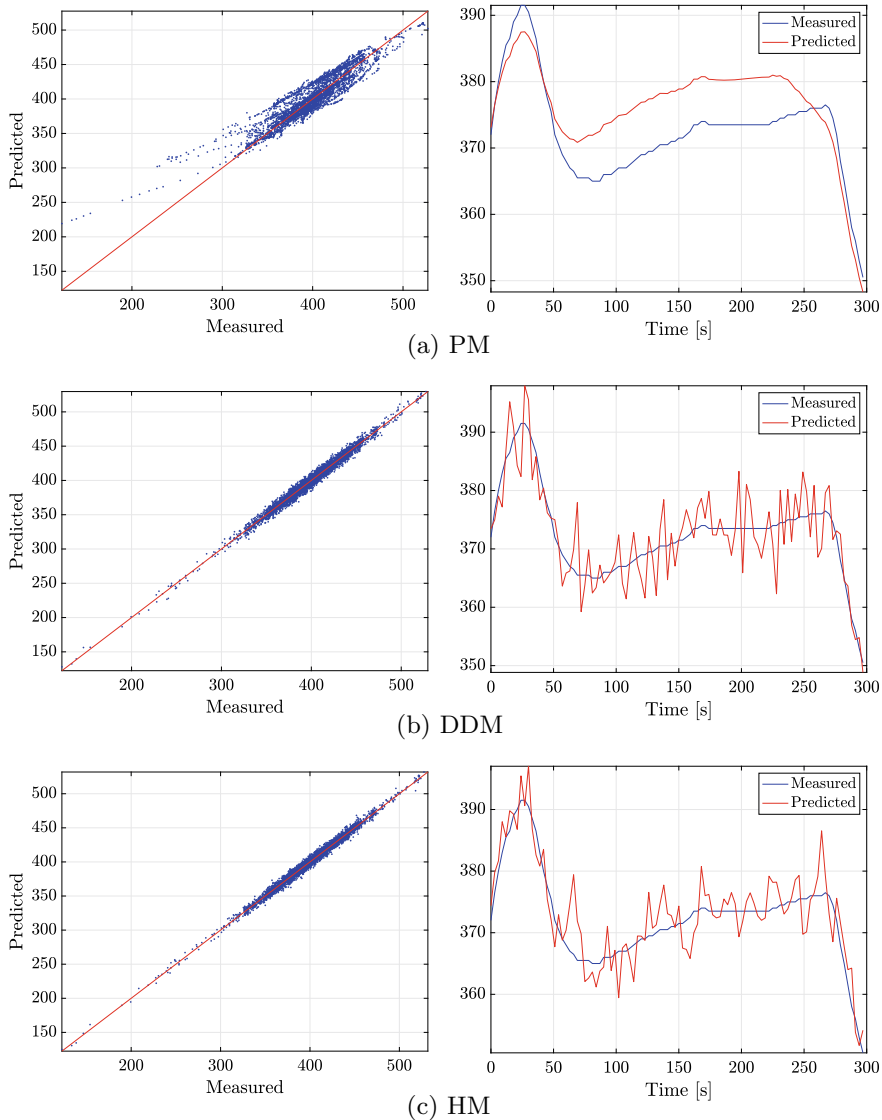
Fig. 6.8 Scatter plot (measured vs. predicted) and trend in time for $T_{t,\text{out}}$ (°C) output feature using the different models (PMs, DDMs, and HMs) with $\Delta = 0$

Fig. 6.9 Scatter plot (measured vs. predicted) and trend in time for T_{er} (°C) output feature using the different models (PMs, DDMs, and HMs) with $\Delta = 0$

(a) DDM

(b) HM

Fig. 6.10 Scatter plot (measured vs. predicted) and trend in time for $\dot{m}_f$ (kg/h) output feature using the different models (DDMs and HMs) with $\Delta = 20$

plot (measured and predicted values) and an example of trend in time (measured and predicted values) for the different targets using the different models (in this case PM, DDM, and HM). Moreover, Figs. 6.10, 6.11, 6.12 and 6.13 report for the value of Δ characterised by the best results in terms of accuracy ($\Delta = 20$) the scatter plots (measured and predicted values) and examples of trend in time (measured and predicted values) for DDM and HM.

Compared to the PM, the proposed DDMs are more accurate in predicting the four targets ($\dot{m}_f$, N_{tc}, $T_{t,out}$, and T_{er}), even without taking into account past information ($\Delta > 0$). A substantial decrease of the errors can be observed from Table 6.8 across all the targets. Considering $\dot{m}_f$, we can observe a MAPE decrease from 26.93% (PM) to 6.30% (DDM), to 4.89% (HM). The same general trend can be reported for N_{tc}, $T_{t,out}$, and T_{er}.

Moreover, when taking into account past information ($\Delta > 0$), from the error metrics reported in Table 6.8 we can observe:

- $\dot{m}_f$ − 90% MAPE reduction from 26.93% ±1.54% to 2.50% ±0.15%
- N_{tc} − 93% MAPE reduction from 15.39% ±0.75% to 0.94% ±0.05%
- $T_{t,out}$ − 80% MAPE reduction from 2.53% ±0.13% to 0.48% ±0.02%
- T_{er} − 88% MAPE reduction from 4.81% ±0.15% to 0.56% ±0.03%

(a) DDM

(b) HM
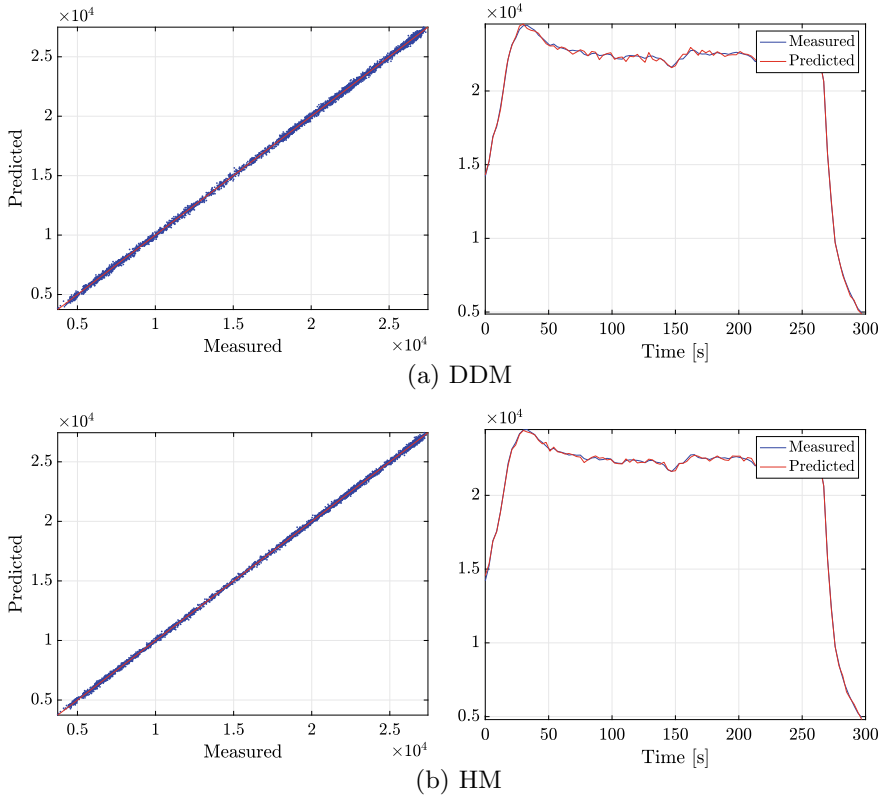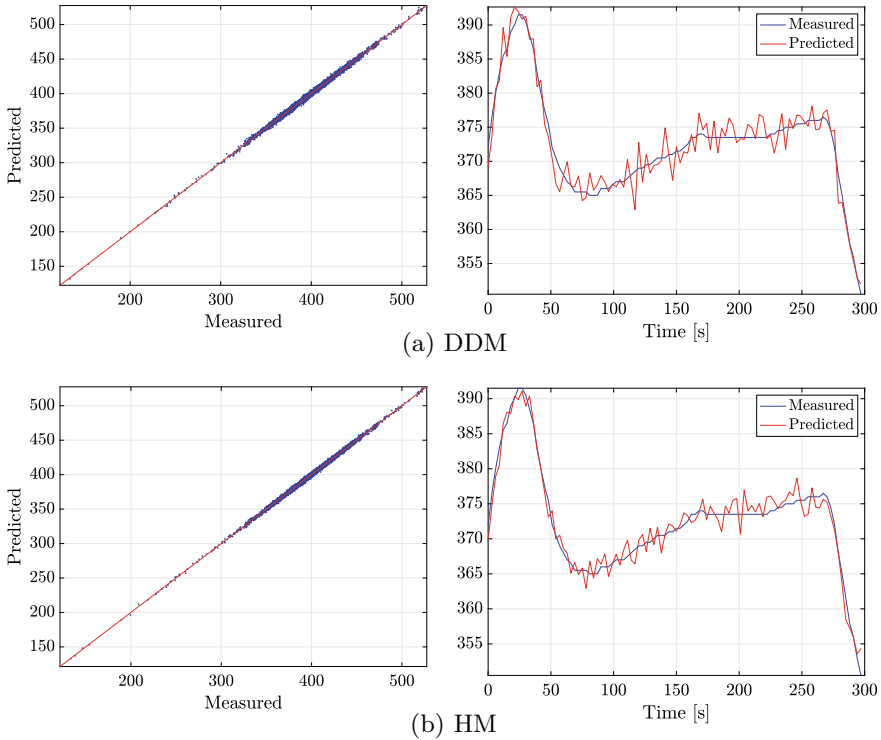
Fig. 6.11 Scatter plot (measured vs. predicted) and trend in time for N_{tc} (°C) output feature using the different models (DDMs and HMs) with $\Delta = 20$

From Figs. 6.6, 6.7, 6.8 and 6.9 it is possible to observe that DDMs are capable of fully capturing the transient behaviour of the fuel consumption (see Fig. 6.6b), the turbocharger rotational speed mechanical transient (see Fig. 6.7b), and the thermodynamic transients of both the turbine outlet gases (see Fig. 6.8b) and exhaust manifold (see Fig. 6.9b). Also from the results depicted in Figs. 6.6, 6.7, 6.8 and 6.9, it can be also observed that the DDMs are characterised by both lower bias and lower variance, with respect to the PM. The optimal time window (Δ) is found for a value equal to 20 seconds. For this value, minimal error metrics among all DDMs occur. According to Table 6.8, for this time window, the MAPE for $\dot{m}_f$ is as low as 1.79% $\pm$ 0.08%, for N_{tc} the MAPE is 0.83% $\pm$ 0.05%, for $T_{t,\text{out}}$ and T_{er} the same metric is identical and equal to 0.40% $\pm$ 0.01%. Furthermore, from the scatter plot of Figs. 6.10a, 6.11a, 6.12a, and 6.13a, it can be observed that minimum variance is achieved.

Table 6.8 Indexes of performances (MAE, MAPE, and PPMCC) of the different models (PMs, DDMs, and HMs) for different $\Delta \in \{0, 10, 20, 30\}$ for the different quantities to predict

| Δ	Model	MAE [°C]	MAPE [%]	PPMCC
Fuel consumption $\dot{m}_f$ [kg/h]				
0	PM	76.62 ± 4.37	26.93 ± 1.54	0.98 ± 0.01
	DDM	24.11 ± 1.39	6.30 ± 0.38	0.99 ± 0.01
	HM	18.64 ± 0.98	4.89 ± 0.17	1.00 ± 0.01
10	DDM	9.55 ± 0.43	2.50 ± 0.15	1.00 ± 0.01
	HM	7.64 ± 0.48	2.01 ± 0.08	1.00 ± 0.01
20	DDM	6.83 ± 0.34	1.79 ± 0.08	1.00 ± 0.01
	HM	5.42 ± 0.25	1.43 ± 0.09	1.00 ± 0.01
30	DDM	11.36 ± 0.57	2.98 ± 0.15	1.00 ± 0.01
	HM	9.09 ± 0.60	2.39 ± 0.12	1.00 ± 0.01
TC rotational speed N_{tc} [rpm]				
0	PM	2090.10 ± 78.43	15.39 ± 0.75	0.97 ± 0.01
	DDM	302.62 ± 21.42	2.18 ± 0.15	1.00 ± 0.01
	HM	214.44 ± 9.54	1.53 ± 0.08	1.00 ± 0.01
10	DDM	130.12 ± 7.63	0.94 ± 0.05	1.00 ± 0.01
	HM	102.22 ± 4.02	0.74 ± 0.04	1.00 ± 0.01
20	DDM	114.57 ± 6.63	0.83 ± 0.05	1.00 ± 0.01
	HM	91.78 ± 4.59	0.66 ± 0.02	1.00 ± 0.01
30	DDM	157.90 ± 7.20	1.13 ± 0.06	1.00 ± 0.01
	HM	124.01 ± 7.58	0.90 ± 0.06	1.00 ± 0.01
Turbine outlet temperature $T_{t,out}$ [°C]				
0	PM	9.66 ± 0.57	2.53 ± 0.13	0.92 ± 0.01
	DDM	3.80 ± 0.20	0.97 ± 0.05	0.99 ± 0.01
	HM	3.18 ± 0.22	0.81 ± 0.05	0.99 ± 0.01
10	DDM	1.89 ± 0.12	0.48 ± 0.02	1.00 ± 0.01
	HM	1.54 ± 0.09	0.39 ± 0.02	1.00 ± 0.01
20	DDM	1.58 ± 0.11	0.40 ± 0.01	1.00 ± 0.01
	HM	1.27 ± 0.04	0.32 ± 0.02	1.00 ± 0.01
30	DDM	2.26 ± 0.11	0.57 ± 0.03	1.00 ± 0.01
	HM	1.76 ± 0.10	0.45 ± 0.02	1.00 ± 0.01
Exhaust manifold temperature T_{er} [°C]				
0	PM	19.92 ± 1.06	4.81 ± 0.15	0.96 ± 0.01
	DDM	5.02 ± 0.19	1.13 ± 0.04	0.99 ± 0.01
	HM	3.94 ± 0.24	0.88 ± 0.05	0.99 ± 0.01
10	DDM	2.51 ± 0.12	0.56 ± 0.03	1.00 ± 0.01
	HM	1.99 ± 0.07	0.45 ± 0.03	1.00 ± 0.01
20	DDM	1.78 ± 0.10	0.40 ± 0.01	1.00 ± 0.01
	HM	1.43 ± 0.05	0.32 ± 0.01	1.00 ± 0.01
30	DDM	3.23 ± 0.19	0.73 ± 0.05	1.00 ± 0.01
	HM	2.57 ± 0.11	0.58 ± 0.03	1.00 ± 0.01

Note that $\Delta = 0$ means that the authors do not exploit time series information from the past, for $\Delta > 0$ there is no PM result

Fig. 6.12 Scatter plot (measured vs. predicted) and trend in time for $T_{t,\text{out}}$ (°C) output feature using the different models (DDMs and HMs) with $\Delta = 20$

It should be noted that, although DDMs are computationally demanding in the training phase, they are characterised by lower computational complexity in the feed-forward phase, as they just require matrix manipulation methods, in contrast with the solution of a system of first order differential equations that the PM requires (see Sect. 6.3.1). The combination of both accurate and fast predictions, makes DDMs an ideal candidate for real-time performance and condition estimation. However, the necessary data to reach this level of performance is rather high as reported in (Cipollini et al. 2018a, b), which makes this type of models applicable only after extensive measurement campaigns have been undertaken. In addition, another disadvantage of DDMs is the lack of interpretability as it is not supported by any physical interpretation (Shawe-Taylor and Cristianini 2004).

To overcome those limitations we proposed the use of HMs. These allow the exploitation of both the mechanistic knowledge of the underlying physical principles from the PM, and any available measurements taken during the operation of the vessel. An advantage of the HMs is their ability to exploit the coarse, but physically supported, predictions of the PM. Therefore, HMs have much smaller requirements regarding the use of actual measurements for the learning phase (Coraddu et al. 2017).

(a) DDM

(b) HM
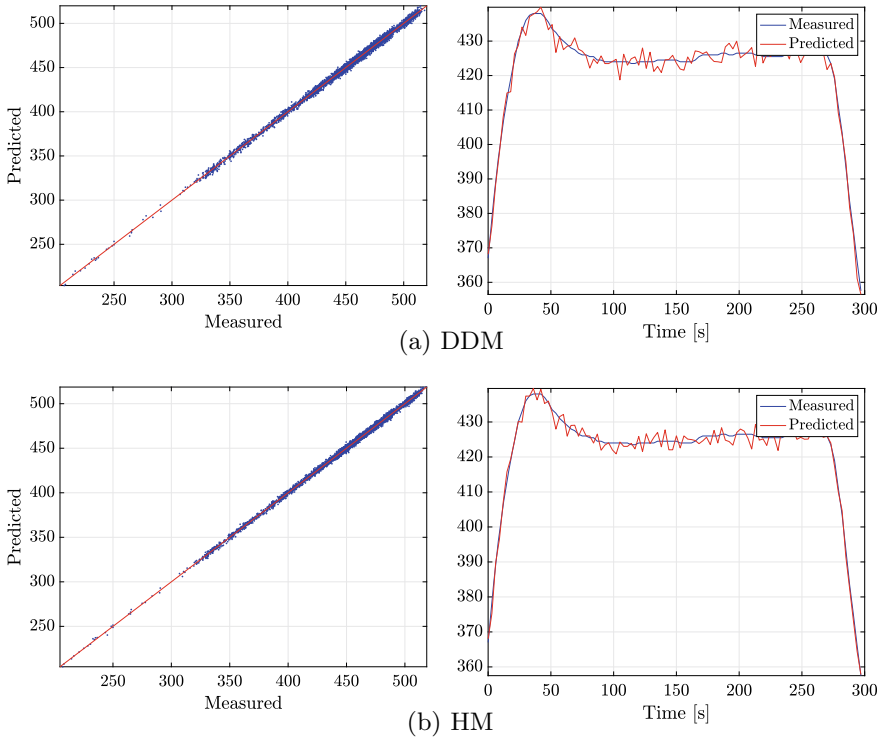
Fig. 6.13 Scatter plot (measured vs. predicted) and trend in time for T_{er} (°C) output feature using the different models (DDMs and HMs) with $\Delta = 20$

While they will still require a measurement campaign in order to be deployed, they can be reliably used already after a few months worth of measurements, in contrast with pure DDMs that would require at least half a year of available data, before they can be exploited.

The novelty introduced by the HMs led to more accurate predictions of the four targets compared to the rest of the models (PM and DDMs), regardless of the time window considered (Δ), as can be seen from Table 6.8. Furthermore, the same table shows that the optimal model is an HM with a time window of 20 seconds, which achieves MAPEs of $1.43\% \pm 0.09\%$ for $\dot{m}_f$, $0.66\% \pm 0.02\%$ for N_{tc}, $0.32\% \pm 0.02\%$ for $T_{t,out}$, and $0.32\% \pm 0.01\%$ for $T_{t,out}$. This is also supported by Figs. 6.10b, 6.11b, 6.12b, and 6.13b, which show representative time-series of the predictions of the four considered targets ($\dot{m}_f$, N_{tc}, $T_{t,out}$, and T_{er}) for time windows of 20 seconds. Finally, it can be noted that the variance has been completely eliminated, whereas the bias has been reduced to near-zero levels.

6.6 Conclusions and Future Perspectives

In this work the authors focused their attention on demonstrating a novel modelling framework for the hybridisation of physical and data driven models. The proposed framework is capable of delivering accurate, reliable, and computationally inexpensive models suitable for real-time performance assessment and condition monitoring applications. State-of-the-art data-driven methods have been presented, able to exploit the information provided by on-board measurements from one Holland Class Oceangoing Patrol Vessel, provided by the Royal Netherlands Navy and Damen Schelde Naval Shipbuilding. First, a 0-D physical model of a medium speed two-stroke diesel engine (MAN 12 V28-33D) was described in detail and validated against measured data. The results reported in Sect. 6.5.1 showed that the automatic calibration processes for stationary operations can provide suitable parameter values to adjust the model's response to the measured signals, capturing the stationary engine operation for a wide span of loads, ranging between 20–100%. The stationary relative errors are in general below 3.5% for the validation data. Nonetheless, the physical model proved to be not accurate enough to capture the engine behaviour in transient conditions. In this respect, the dynamic validation reported in Sect. 6.5.2 showed that the physical model model is capable of following the measured engine signals during transients, nonetheless, its response is not accurate. Moreover, its complexity depend upon computational requirements that are sometimes prohibitive, preventing the use of the physical model in real time applications.

Therefore, data-driven models have been discussed and proposed in Sect. 6.3.2, for predicting the behaviour of the engine, with a focus on four different targets: (i) fuel consumption, (ii) turbocharger rotational speed, (iii) turbine outlet temperature, and iv) exhaust receiver temperature. The models proved to be very accurate, with the enhanced capability of exploiting time series information from the past, achieving relative errors below 1% on the validation data, across all the considered output features. However, due to their nature, these data-driven models are hard to interpret.

To overcome the limitations of both the physical and the data-driven models, we proposed a hybrid approach that can take into consideration past information, capable of improving accuracy, easily interpreted, and have low computational time requirements. The hybridisation of physical and data driven models proved to be extremely accurate, achieving even lower errors when compared to the simple data-driven approach. These hybrid models can potentially also be used to improve accuracy of predictions for operation in other conditions than the measured ones, as purely data-driven models cannot be used for extrapolation, but the physical model contribution will improve hybrid model performance during extrapolation. While the hybrid approach will still require a measurement campaign in order to be deployed, this approach can be reliably used based on a significantly smaller dataset in comparison with the pure data-driven models, for the same average error, as shown in Sect. 6.5.2.

References

Ahmed R, El Sayed M, Gadsden SA, Tjong J, Habibi S (2015) Automotive internal-combustion-engine fault detection and classification using artificial neural network techniques. IEEE Trans Veh Technol 64(1):21–33

Argyriou A, Evgeniou T, Pontil M (2008) Convex multi-task feature learning. Mach Learn 73(3):243–272

Audet C, Dennis JE (2006) Mesh adaptive direct search algorithms for constrained optimization. SIAM J Optim 17(1):188–217

Audet C, Custódio AL, Dennis JE (2008) Erratum: mesh adaptive direct search algorithms for constrained optimization. SIAM J Optim 18(4):1501–1503

Bakker B, Heskes T (2003) Task clustering and gating for bayesian multitask learning. J Mach Learn Res 4:83–99

Baldi F, Johnson H, Gabrielii C, Andersson K (2014) Energy and exergy analysis of ship energy systems-the case study of a chemical tanker. In: ECOS, international conference on efficiency, cost, optimization, simulation and environmental impact of energy systems

Baldi F, Theotokatos G, Andersson K (2015) Development of a combined mean value-zero dimensional model and application for a large marine four-stroke diesel engine simulation. Appl Energy 154:402–415

Baxter J (2000) A model of inductive bias learning. J Artif Intel Res 12:149–198

Bidarvatan M, Thakkar V, Shahbakhti M, Bahri B, Aziz AA (2014) Grey-box modeling of hcci engines. Appl Therm Eng 70(1):397–409

Bouman EA, Lindstad E, Rialland AI, Strømman AH (2017) State-of-the-art technologies, measures, and potential for reducing ghg emissions from shipping-a review. Transp Res Part D: Transp Environ 52:408–421

Caruana R (1997) Multitask learning. Mach Learn 28(1):41–75

Chen S, Flynn P (1965) Development of a single cylinder compression ignition research engine. Technical report, SAE Technical Paper

Chiong MC, Kang HS, Shaharuddin N, Ma S et al (2021) Challenges and opportunities of marine propulsion with alternative fuels. Renew Sustain Energy Rev 149:111397

Cipollini F, Oneto L, Coraddu A, Murphy AJ, Anguita D (2018) Condition-based maintenance of naval propulsion systems with supervised data analysis. Ocean Eng 149:268–278

Cipollini F, Oneto L, Coraddu A, Murphy AJ, Anguita D (2018) Condition-based maintenance of naval propulsion systems: data analysis with minimal feedback. Reliab Eng Syst Safety 177:12–23

Commission European (2013a) Integrating maritime transport in the eu's greenhouse gas reduction policies: Communication from the commission to the european parliament, the council, the european economic and social committee and the committee of the regions. Technical report, European Union

Commission European (2013b) Proposal for a regulation of the european parliament and of the council on the monitoring, reporting and verification of carbon dioxide emissions from maritime transport and amending regulation (eu) no 525/2013. Technical report, European Union

Committee M.E.P. (2011) Resolution mepc. 203 (62); amendments to the annex of the protocol of (1997) to amend the international convention for the prevention of pollution from ships, 1973, as modified by the protocol of 1978 relating thereto. Technical report, International Maritime Organization

Conn AR, Scheinberg K, Vicente LN (2009) Introduction to derivative-free optimization. SIAM

Coraddu A, Oneto L, Ghio A, Savio S, Anguita D, Figari M (2016) Machine learning approaches for improving condition-based maintenance of naval propulsion plants. Proc Inst Mechan Eng Part M: J Eng Marit Environ 230(1):136–153

Coraddu A, Oneto L, Baldi F, Anguita D (2017) Vessels fuel consumption forecast and trim optimisation: a data analytics perspective. Ocean Eng 130:351–370

Coraddu A, Kalikatzarakis M, Oneto L, Meijn GJ, Godjevac M, Geertsmad RD (2018) Ship diesel engine performance modelling with combined physical and machine learning approach. In: International Naval engineering conference and exhibition

Coraddu A, Oneto L, Baldi F, Cipollini F, Atlar M, Savio S (2019a) Data-driven ship digital twin for estimating the speed loss caused by the marine fouling. Ocean Eng 186:106063

Coraddu A, Lim S, Oneto L, Pazouki K, Norman R, Murphy AJ (2019b) A novelty detection approach to diagnosing hull and propeller fouling. Ocean Eng 176:65–73

Coraddu A, Oneto L, de Maya BN, Kurt R (2020) Determining the most influential human factors in maritime accidents: a data-driven approach. Ocean Eng 211:107588

Coraddu A, Oneto L, Cipollini F, Kalikatzarakis M, Meijn GJ, Geertsma R (2021a) Physical, data-driven and hybrid approaches to model engine exhaust gas temperatures in operational conditions. Ships Offshore Struct 1–22

Coraddu A, Oneto L, Ilardi D, Stoumpos S, Theotokatos G (2021b) Marine dual fuel engines monitoring in the wild through weakly supervised data analytics. Eng Appl Artif Intel 100:104179

Cristianini N, Shawe-Taylor J (2000) An introduction to support vector machines and other Kernel-based learning methods. Cambridge University Press, Cambridge

Dahl J, Wassén H, Santin O, Herceg M, Lansky L, Pekar J, Pachner D (2018) Model predictive control of a diesel engine with turbo compound and exhaust after-treatment constraints. IFAC-PapersOnLine 51(31):349–354

Descieux D, Feidt M (2007) One zone thermodynamic model simulation of an ignition compression engine. Appl Therm Eng 27(8–9):1457–1466

Ding Y, Stapersma D, Knoll H, Grimmelius H, Netherland T (2010) Characterising heat release in a diesel engine: a comparison between seiliger process and vibe model. In: CIMAC world congress on combustion engine technology

Evgeniou T, Pontil M (2004) Regularized multi-task learning. In: ACM SIGKDD international conference on knowledge discovery and data mining

Fagerholt K, Psaraftis HN (2015) On two speed optimization problems for ships that sail in and out of emission control areas. Transp Res Part D: Transp Environ 39:56–64

Fernández-Delgado M, Cernadas E, Barro S, Amorim D (2014) Do we need hundreds of classifiers to solve real world classification problems? J Mach Learn Res 15(1):3133–3181

Floudas CA, Pardalos P (2008) Encyclopedia of optimization. Springer, Berlin

Galindo J, Climent H, Plá B, Jiménez VD (2011) Correlations for wiebe function parameters for combustion simulation in two-stroke small engines. Appl Therm Eng 31(6–7):1190–1199

Galinier P, Hamiez JP, Hao JK, Porumbel D (2013) Handbook of optimization. Springer, Berlin

García-Martos C, Rodríguez J, Sánchez MJ (2013) Modelling and forecasting fossil fuels, co2 and electricity prices and their volatilities. Appl Energy 101:363–375

Geertsma RD, Negenborn RR, Visser K, Loonstijn MA, Hopman JJ (2017) Pitch control for ships with diesel mechanical and hybrid propulsion: modelling, validation and performance quantification. Appl Energy 206:1609–1631

Geertsma RD, Visser K, Negenborn RR (2018) Adaptive pitch control for ships with diesel mechanical and hybrid propulsion. Appl Energy 228:2490–2509

Ghojel JI (2010) Review of the development and applications of the wiebe function: a tribute to the contribution of ivan wiebe to engine research. Int J Eng Res 11(4):297–312

Gogoi TK, Baruah DC (2010) A cycle simulation model for predicting the performance of a diesel engine fuelled by diesel and biodiesel blends. Energy 35(3):1317–1323

Goodfellow I, Bengio Y, Courville A (2016) Deep learning. MIT Press, Cambridge

Grimmelius HT (2003) Simulation models in marine engineering: from training to concept explo-
    ration. In: International EuroConference on Computer and IT Applications in the Maritime Indus-
    tries

Grimmelius H, Boonen EJ, Nicolai H, Stapersma D (2010) The integration of mean value first
    principle diesel engine models in dynamic waste heat and cooling load analysis. In: CIMAC
    World Congress on Combustion Engine Technology

Grimmelius H, Mesbahi E, Schulten P, Stapersma D (2007) The use of diesel engine simulation
    models in ship propulsion plant design and operation. In: CIMAC international council on com-
    bustion engines

Guan C, Theotokatos G, Zhou P, Chen H (2014) Computational investigation of a large containership
    propulsion engine operation at slow steaming conditions. Appl Energy 130:370–383

Guan C, Theotokatos G, Chen H (2015) Analysis of two stroke marine diesel engine operation
    including turbocharger cut-out by using a zero-dimensional model. Energies 8(6):5738–5764

Gucwa M, Schäfer A (2013) The impact of scale on energy intensity in freight transportation. Transp
    Res Part D: Transp Environ 23:41–49

Guzzella L, Onder C (2009) Introduction to modeling and control of internal combustion engine
    systems. Springer, Berlin

Hamilton JD (2020) Time series analysis. Princeton University Press, Princeton

Hanson RK, Salimian S (1984) Survey of rate constants in the n/h/o system. Combust Chem 361–421

Hao C, Lu Z, Feng Y, Bai H, Wen M, Wang T (2021) Optimization of fuel/air mixing and combustion
    process in a heavy-duty diesel engine using fuel split device. Appl Therm Eng 186:116458

He Y, Lin C (2007) Development and validation of a mean value engine model for integrated engine
    and control system simulation. Technical report, SAE Technical Paper

Heywood JB (1988) Internal combustion engines fundamentals. McGraw-Hill, New York

Johnson K, Mollenhauer K, Tschoke H (2010) Handbook of diesel engines. Springer, Berlin

Kamal K, Hui C (2013) A semi-experimental modeling approach for a large two-stroke marine
    diesel engine simulation. In: CIMAC world congress on combustion engine technology

Keerthi SS, Lin CJ (2003) Asymptotic behaviors of support vector machines with gaussian kernel.
    Neural Comput 15(7):1667–1689

Kökkülünk G, Parlak A, Erdem H (2016) Determination of performance degradation of a marine
    diesel engine by using curve based approach. Appl Therm Eng 108:1136–1146

Larsen U, Pierobon L, Baldi F, Haglind F, Ivarsson A (2015) Development of a model for the
    prediction of the fuel consumption and nitrogen oxides emission trade-off for large ships. Energy
    80:545–555

Lee B, Jung D, Kim Y, van Nieuwstadt M (2013) Thermodynamics-based mean value model for
    diesel combustion. J Eng Gas Turb Power **135**(9)

Lewis RM, Torczon V, Trosset MW (2000) Direct search methods: then and now. J Comput Appl
    Math 124(1–2):191–207

Lindstad H, Eskeland GS (2015) Low carbon maritime transport: how speed, size and slenderness
    amounts to substantial capital energy substitution. Transp Res Part D: Transp Environ 41:244–256

Lindstad H, Verbeek R, Blok M, van Zyl S, Hübscher A, Kramer H, Purwanto J, Ivanova O,
    Boonman H (2015) Ghg emission reduction potential of eu-related maritime transport and its
    impacts. Technical report, Van Mourik Broekmanweg

Lion S, Vlaskos I, Taccani R (2020) A review of emissions reduction technologies for low and
    medium speed marine diesel engines and their potential for waste heat recovery. Energy Convers
    Manage 207:112553

Liu Z, Zuo Q, Wu G, Li Y (2018) An artificial neural network developed for predicting of perfor-
    mance and emissions of a spark ignition engine fueled with butanol-gasoline blends. Adv Mechan
    Eng 10(1):1687814017748438

Livanos G, Papalambrou G, Kyrtatos NP, Christou A (2007) Electronic engine control for ice
    operation of tankers. In: CIMAC world congress on combustion engine technology

Llamas X, Eriksson L (2018) Control-oriented modeling of two-stroke diesel engines with exhaust
    gas recirculation for marine applications. J Eng Marit Environ, Proc Inst Mechan Eng Part M

Llamas X, Eriksson L (2019) Control-oriented modeling of two-stroke diesel engines with exhaust gas recirculation for marine applications. Proc Inst Mechan Eng Part M: J Eng Marit Environ 233(2):551–574

Malkhede DN, Seth B, Dhariwal HC (2005) Mean value model and control of a marine turbocharged diesel engine. Technical report, SAE Technical Paper

Maroteaux F, Saad C (2015) Combined mean value engine model and crank angle resolved in-cylinder modeling with nox emissions model for real-time diesel engine simulations at high engine speed. Energy 88:515–527

Martí R (2003) Multi-start methods. In: Handbook of metaheuristics

McBride BJ, Zehe MJ (2002) NASA Glenn coefficients for calculating thermodynamic properties of individual species. Natl Aeronaut Space Adm

Merker GP, Schwarz C, Stiesch G, Otto F (2005) Simulating combustion: simulation of combustion and pollutant formation for engine development. Springer, Berlin

Miglianti F, Cipollini F, Oneto L, Tani G, Viviani M (2019) Model scale cavitation noise spectra prediction: combining physical knowledge with data science. Ocean Eng 178:185–203

Miglianti L, Cipollini F, Oneto L, Tani G, Gaggero S, Coraddu A, Viviani M (2020) Predicting the cavitating marine propeller noise at design stage: A deep learning based approach. Ocean Eng 209:107481

Mishra C, Subbarao PMV (2021) A comparative study of physics based grey box and neural network trained black box dynamic models in an rcci engine control parameter prediction. Technical report, SAE Technical Paper

Miyamoto N, Chikahisa T, Murayama T, Sawyer R (1985) Description and analysis of diesel engine rate of combustion and performance using wiebe's functions. SAE Trans 622–633

Mohammadkhani F, Yari M, Ranjbar F (2019) A zero-dimensional model for simulation of a diesel engine and exergoeconomic analysis of waste heat recovery from its exhaust and coolant employing a high-temperature kalina cycle. Energy Convers Manage 198:111782

Namigtle-Jiménez A, Escobar-Jiménez RF, Gómez-Aguilar JF, García-Beltrán CD, Téllez-Anguiano AC (2020) Online ANN-based fault diagnosis implementation using an fpga: application in the EFI system of a vehicle. ISA Trans 100:358–372

Ni P, Wang X, Li H (2020) A review on regulations, current status, effects and reduction strategies of emissions for marine diesel engines. Fuel 279:118477

Nikzadfar K, Shamekhi AH (2014) Investigating the relative contribution of operational parameters on performance and emissions of a common-rail diesel engine using neural network. Fuel 125:116–128

Nikzadfar K, Shamekhi AH (2015) An extended mean value model (emvm) for control-oriented modeling of diesel engines transient performance and emissions. Fuel 154:275–292

Oberkampf WL, Trucano TG (2002) Verification and validation in computational fluid dynamics. Progr Aerosp Sci 38(3):209–272

Oberkampf WL, Trucano TG, Hirsch C (2004) Verification, validation, and predictive capability in computational engineering and physics. Appl Mechan Rev 57(5):345–384

Oneto L (2020) Model selection and error estimation in a nutshell. Springer, Berlin

Oneto L, Ghio A, Ridella S, Anguita D (2015) Support vector machines and strictly positive definite kernel: the regularization hyperparameter is more important than the kernel hyperparameters. In: IEEE international joint conference on neural networks (IJCNN)

Oneto L, Anguita D, Coraddu A, Cleophas T, Xepapa K (2016) Vessel monitoring and design in industry 4.0: a data driven perspective. In: 2016 IEEE 2nd international forum on research and technologies for society and industry leveraging a better tomorrow (RTSI), pp 1–6. IEEE

Özener O, Yüksek L, Özkan M (2013) Artificial neural network approach to predicting engine-out emissions and performance parameters of a turbo charged diesel engine. Therm Sci 17(1):153–166

Palmer KA, Bollas GM (2019) Active fault diagnosis for uncertain systems using optimal test designs and detection through classification. ISA Trans 93:354–369

Psaraftis HN, Kontovas CA (2014) Ship speed optimization: concepts, models and combined speed-routing scenarios. Transp Res Part C: Emerg Technol 44:52–69

Rakopoulos CD, Hountalas DT, Tzanos EI, Taklis GN (1994) A fast algorithm for calculating the composition of diesel combustion products using 11 species chemical equilibrium scheme. Adv Eng Softw 19(2):109–119

Rakopoulos CD, Rakopoulos DC, Mavropoulos GC, Giakoumis EG (2004) Experimental and theoretical study of the short term response temperature transients in the cylinder walls of a diesel engine at various operating conditions. Appl Therm Eng 24(5–6):679–702

Rosasco L, De Vito E, Caponnetto A, Piana M, Verri A (2004) Are loss functions all the same? Neural Comput 16(5):1063–1076

Sapra H, Godjevac M, Visser K, Stapersma D, Dijkstra C (2017) Experimental and simulation-based investigations of marine diesel engine performance against static back pressure. Appl Energy 204:78–92

Sapra H, Godjevac M, De Vos P, Van Sluijs W, Linden Y, Visser K (2020) Hydrogen-natural gas combustion in a marine lean-burn si engine: a comparitive analysis of seiliger and double wiebe function-based zero-dimensional modelling. Energy Convers Manage 207:112494

Scholkopf B (2001) The kernel trick for distances. In: Advances in neural information processing systems, pp 301–307

Schölkopf B, Herbrich R, Smola AJ (2001) A generalized representer theorem. In: Computat Learn Theor

Shalev-Shwartz S, Ben-David S (2014) Understanding machine learning: from theory to algorithms. Cambridge University Press, Cambridge

Shao L, Mahajan A, Schreck T, Lehmann DJ (2017) Interactive regression lens for exploring scatter plots. Comput Gr Forum

Shawe-Taylor J, Cristianini N (2004) Kernel methods for pattern analysis. Cambridge University Press, Cambridge

Shin S, Lee Y, Kim M, Park J, Lee S, Min K (2020) Deep neural network model with bayesian hyperparameter optimization for prediction of nox at transient conditions in a diesel engine. Eng Appl Artif Intel 94:103761

Sitkei G (1963) Über den dieselmotorischen zündverzug. MTZ 24(6):190–194

Stoer J, Bulirsch R (2013) Introduction to numerical analysis, vol 12. Springer, Berlin

Stoumpos S, Theotokatos G, Boulougouris E, Vassalos D, Lazakis I, Livanos G (2018) Marine dual fuel engine modelling and parametric investigation of engine settings effect on performance-emissions trade-offs. Ocean Eng 157:376–386

Stoumpos S, Theotokatos G, Mavrelos C, Boulougouris E (2020) Towards marine dual fuel engines digital twins-integrated modelling of thermodynamic processes and control system functions. J Marine Sci Eng 8(3):200

Sui C, Song E, Stapersma D, Ding Y (2017) Mean value modelling of diesel engine combustion based on parameterized finite stage cylinder process. Ocean Eng 136:218–232

Syed J, Baig RU, Algarni S, Murthy S, Masood M, Inamurrahman M (2017) Artificial neural network modeling of a hydrogen dual fueled diesel engine characteristics: an experiment approach. Int J Hydr Energy 42(21):14750–14774

Tang Y, Zhang J, Gan H, Jia B, Xia Y (2017) Development of a real-time two-stroke marine diesel engine model with in-cylinder pressure prediction capability. Appl Energy 194:55–70

Theotokatos G (2008) Ship propulsion plant transient response investigation using a mean value engine model. Int J Energy 2(4):66–74

Theotokatos G (2010) On the cycle mean value modelling of a large two-stroke marine diesel engine. Proc Inst Mechan Eng Part M: J Eng Marit Environ 224(3):193–205

Theotokatos G, Kyrtatos NP (2003) Investigation of a large high-speed diesel engine transient behavior including compressor surging and emergency shutdown. J Eng Gas Turb Power 125(2):580–589

Theotokatos G, Tzelepis V (2015) A computational study on the performance and emission parameters mapping of a ship propulsion system. Proc Instit Mechan Eng Part M: J Eng Marit Environ 229(1):58–76

Theotokatos G, Guan C, Chen H, Lazakis I (2018) Development of an extended mean value engine model for predicting the marine two-stroke engine operation at varying settings. Energy 143:533–545

Tikhonov AN, Arsenin VY (1979) Methods for solving III-posed problems. Nauka, Moscow

Tillig F, Mao W, Ringsberg J (2015) Systems modelling for energy-efficient shipping. Technical report, Chalmers University of Technology (2015)

Torczon V (1997) On the convergence of pattern search algorithms. SIAM J Optim 7(1):1–25

Vapnik VN (1998) Statistical learning theory. Wiley, New York

Vovk V (2013) Kernel ridge regression. In: Empirical inference

Wahlström J, Eriksson L (2011) Modelling diesel engines with a variable-geometry turbocharger and exhaust gas recirculation by optimization of model parameters for capturing non-linear system dynamics. Proc Inst Mechan Eng Part D: J Automob Eng 225(7):960–986

Wainberg M, Alipanahi B, Frey BJ (2016) Are random forests truly the best classifiers? J Mach Learn Res 17(1):3837–3841

Wang J, Wang Z, Stetsyuk V, Ma X, Gu F, Li W (2019) Exploiting bayesian networks for fault isolation: a diagnostic case study of diesel fuel injection system. ISA Trans 86:276–286

Wang H, Gan H, Theotokatos G (2020a) Parametric investigation of pre-injection on the combustion, knocking and emissions behaviour of a large marine four-stroke dual-fuel engine. Fuel 281:118744

Wang YS, Liu NN, Guo H, Wang XL (2020b) An engine-fault-diagnosis system based on sound intensity analysis and wavelet packet pre-processing neural network. Eng Appl Artif Intel 94:103765

Wang R, Chen H, Guan C (2021) Random convolutional neural network structure: an intelligent health monitoring scheme for diesel engines. Measurement 171:108786

Watson N, Janota M (1982) Turbocharging the internal combustion engine. Macmillan International Higher Education

Wen M, Pacino D, Kontovas CA, Psaraftis HN (2017) A multiple ship routing and speed optimization problem under time, cost and environmental objectives. Transp Res Part D: Transport Environ 52:303–321

Willmott CJ, Matsuura K (2005) Advantages of the mean absolute error (mae) over the root mean square error (rmse) in assessing average model performance. Clim Res 30(1):79–82

Woschni G (1968) A universally applicable equation for the instantaneous heat transfer coefficient in the internal combustion engine. SAE Trans 3065–3083

Woschni G, Anisits F (1973) Eine methode zur vorausberechnung der anderung des brennverlaufs mittelschnellaufender dieselmotoren bei geaenderten betriebsbedingungen. Motortech 34(4):106–115

Xing H, Spence S, Chen H (2020) A comprehensive review on countermeasures for CO2 emissions from ships. Renew Sustain Energy Rev 134:110222

Young DM (2003) Iterative solution of large linear systems. Dover Publications, Mineola

Yu H, Fang Z, Fu X, Liu J, Chen J (2021) Literature review on emission control-based ship voyage optimization. Transp Res Part D: Transp Environ 93:102768

Zheng A, Casari A (2018) Feature engineering for machine learning: principles and techniques for data scientists. O'Reilly Media, Inc

Zis T, Psaraftis HN (2018) Operational measures and logistical considerations for the decarbonisation of maritime transport. In: hEART 2018: 7th Symposium of the European Association for Research in Transportation

Zis T, Psaraftis HN, Ding L (2020) Ship weather routing: a taxonomy and survey. Ocean Eng 213:107697